https://doi.org/10.5194/egusphere-2026-2441
Preprint. Discussion started: 2 July 2026

A CFD-based parameterization approach for correcting vehicle-mounted three-dimensional instantaneous wind measurements

Keyu Chen[1], Yanrong Yang[2], Yufei Huang[3], Yuheng Zhang[4], Jietao Zhou[1], Haijiong Sun[1], Chang Liu [1], Ling Kang[1], Keding Lu[1], Zhijun Wu[1], and Shao-Meng Li [1*]

[1]College of Environmental Sciences and Engineering, Peking University, Beijing 100871, China
[2]Key Lab. for Restoration and Reconstruction of Degraded Ecosystems in Northwestern China of Ministry of Education, School of Ecology and Environment, Ningxia University, Yinchuan 750021, China
[3]Shenzhen Smart City Technology Development Group Co., Ltd., Shenzhen 518038, China
[4]CNPC Research Institute of Safety and Environmental Technology, Beijing 102206, China

Correspondence to: Shao-Meng Li (shaomeng.li@pku.edu.cn)

Abstract. Near-surface three-dimensional wind vectors are essential meteorological variables in atmospheric boundary layer research and environmental monitoring. Vehicle-mounted mobile wind measurement platforms enable observations of near-surface wind fields with high spatial resolutions over relatively large spatial domains. However, vehicle-induced flow distortion, platform motion, and attitude variations introduce substantial interference into vehicle-mounted wind measurements, resulting in systematic deviations of the measured wind vectors from the true ambient wind field. To obtain accurate three-dimensional wind measurements, this study proposes a vehicle-mounted instantaneous wind correction method based on a CFD-derived parameterization scheme. A set of parameterized CFD simulations is conducted within a unified computational domain under multiple wind speeds and directions to establish a mapping between the true inflow wind and the flow-distorted wind measured by vehicle-mounted anemometer. The correction framework further accounts for the effects of vehicle attitude variations and vehicle translation. Based on field comparison experiments, the corrected vehicle-mounted wind speed, wind direction, and vertical wind component show substantially improved agreements with ground-based reference observations under headwind conditions. Under tailwind conditions, the correction performance is reduced but remains superior to uncorrected measurements. Contribution analyses indicate that flow distortion is the dominant source of measurement error, whereas the contribution of attitude variations is generally smaller but can become more evident under low wind speed conditions or during more dynamic vehicle motions. The proposed method provides an efficient and extensible approach for vehicle-mounted three-dimensional wind measurements in complex near-surface wind environments.

1 Introduction

Near-surface wind vectors are key meteorological variables in atmospheric boundary layer dynamics and play an important role in urban meteorological modelling and forecasting (Grimmond and Oke, 1999; Mochida and Lun, 2008), surface–atmosphere energy and momentum exchange (Foken, 2006), atmospheric pollutant transport and dispersion (Seinfeld and Pandis, 2016; Li et al., 2017), as well as environmental monitoring and air quality assessment (Apte et al., 2017; Erland et al.,

https://doi.org/10.5194/egusphere-2026-2441
Preprint. Discussion started: 2 July 2026

2022). Within the near-surface layer, atmospheric flow fields are influenced by a combination of factors, including terrain variability, surface roughness, vegetation distribution, and built structures, and therefore often exhibit pronounced temporal variability and spatial heterogeneity (Grimmond and Oke, 1999; Zajic et al., 2015; Mochida et al., 2008; Lu et al., 2024). However, the accurate wind measurements covering large and complex spatial domains present major challenges to boundary layer research; limited number of fixed meteorological stations and their typically sparse spatial distribution make it difficult for such observations to adequately represent near-surface wind field structures at high spatial resolution (Miller and Gordon, 2022). To address the limited spatial representativeness of fixed observations, wind measurement approaches based on mobile platforms have attracted increasing attention in recent years (Belusic et al., 2014; Wagner et al., 2019). By mounting sensors including anemometers on various vehicle platforms, including passenger cars, sport utility vehicles, trucks, and vans, near-surface wind fields can be continuously measured during vehicle operation, enabling wind observations with high spatial resolutions along roads and at the regional scale (Hanlon and Risk, 2020; Miller and Gordon, 2022). At present, such measurement approaches have been widely applied in mobile meteorological observations (Straka et al., 1996), studies of near-surface turbulence characteristics (Gordon et al., 2012; Belusic et al., 2014; Miller et al., 2019), as well as monitoring of air pollutant and greenhouse gas emissions (Brantley et al., 2014; Apte et al., 2017; Edie et al., 2020).

Compared with fixed-station observations, mobile wind field measurements offer greater flexibility, allowing dynamic deployment according to observational needs and coverage of a wider spatial domain. However, during vehicle motion, wind vector measurements on mobile platforms are inevitably affected by air flow streams introduced by vehicle motion and geometric effects. As the free stream approaches the anemometer mounted on the vehicle, it undergoes complex acceleration, deceleration, deflection processes (Moat et al., 2005) as well as compression and decompression near the vehicle surfaces, leading to systematic deviations of the measured wind vectors from the true ambient wind field. In addition, vehicle-mounted anemometers measure the wind velocity relative to the moving platform rather than the ambient flow. Belušić et al. (2014) pointed out that under typical road-driving conditions, vehicle speed is often approximately an order of magnitude higher than the true wind speeds, such that flow distortion can substantially alter the measured total wind vector. Houston et al. (2016) installed a two-dimensional anemometer on the roof of a Dodge Caravan at a height of approximately 1.8 m above the vehicle roof (3.3 m above ground level) and evaluated wind speed biases at this location using computational fluid dynamic (CFD) simulations. Their results showed that wind speed was overestimated by more than 4% under headwind conditions, while the overestimation exceeded 9% under crosswind conditions. To mitigate such measurement biases, previous studies have suggested placing anemometers as far as possible from the vehicle body and at the highest feasible installation height (Straka et al., 1996). Using CFD simulations, Hanlon and Risk (2020) further analysed the flow field above a Toyota Tacoma under headwind conditions with a yaw angle of 0°. Their results indicated that, to limit wind speed bias to within 1%, the anemometer needed to be installed at a height of 4.36 m above the vehicle. In addition, wind direction was found to have a more pronounced influence on measurement bias than wind speed itself. However, under practical urban road conditions or on highways where overhead obstacles such as tree branches, power lines, traffic lights, and bridge crossings are common, vehicle and its overload height must be constrained to satisfy safety requirements, making it difficult to place anemometers arbitrarily high above or

https://doi.org/10.5194/egusphere-2026-2441
Preprint. Discussion started: 2 July 2026

far away from the vehicle body (Miller and Gordon, 2022). Furthermore, vehicle three-dimensional attitude changes during driving due to directional changes, body bumps and vibrations from uneven road surfaces, and tilts from sloped roads can all cause false wind sensor signals that must also be corrected for. Consequently, sensor placement optimization alone is insufficient to fully eliminate the effects of flow distortion, and a systematic correction of wind measurements from mobile platforms is required.

In studies of shipborne wind measurements (Moat et al., 2006; Griessbaum et al., 2010; Hu et al., 2019) and unmanned aerial vehicle wind measurements (Yang et al., 2025), relatively mature correction approaches are typically based on CFD simulations to numerically reconstruct the flow field around the platform and to derive wind speed correction functions accordingly. In contrast, studies of correction schemes for vehicle-mounted wind measurements still rely largely on empirical assumptions (Miller and Gordon, 2022). The correction scheme of Belušić et al. (2014) and Miller et al. (2019) is based on several core assumptions, namely that a vehicle travels along the same route in opposite directions at the same driving speed and over the same distance, while the true ambient wind speed and wind direction remain constant during the measurement period and the mean vertical wind velocity can be approximated as zero, allowing the correction of the measured wind velocities. However, this approach requires a high degree of stationarity in the ambient wind field during measurement and may therefore mainly be applicable to the correction of the mean wind. Its applicability to instantaneous wind measurements or non-stationary flow conditions remains limited. To address such a gap, alternative approaches to wind correction schemes, such as based on CFD simulations, must be developed for vehicle-based wind measurements. To the best of our knowledge, Hanlon and Risk (2020) represent the only study that has established a correction scheme for vehicle-mounted two-dimensional wind measurements using CFD simulations under their specific vehicle-sensor configuration and vehicle operation conditions, with a simulated range of relative wind speeds restricted to 40–100 km h^{-1}, primarily targeting high-speed driving conditions. No consideration was given to the impacts of vehicle attitude changes. As a result, this approach is not directly applicable to wind measurements under typical urban street conditions and cannot resolve 3-d wind vectors. Furthermore, accurate reconstruction of arbitrary inflow wind directions requires correction methods to be applicable across the full range of wind directions. However, within a CFD simulation framework, changing the inflow direction typically necessitates reconstruction of the computational domain and repeated simulations, resulting in high computational costs and limited practical efficiency (Hanlon and Risk, 2020; Yang et al., 2025). Existing correction approaches for mobile platforms commonly suffer from limited wind direction coverage, an insufficient number of simulated cases, and relatively coarse flow field resolution (Hu et al., 2019; Hanlon and Risk, 2020), which hampers a systematic characterization of flow distortion effects on anemometer measurements under different inflow conditions. Therefore, there is a clear need to develop an efficient and accurate modelling framework tailored to vehicle-mounted platforms, capable of achieving reliable three-dimensional instantaneous wind correction while maintaining computational feasibility.

To address the aforementioned challenges, this study developed a three-dimensional wind correction method for vehicle-mounted three-dimensional wind measurements based on a CFD-derived parameterization scheme that supports automated simulations for a large number of cases. On the basis of the parameterized CFD results, the effects of vehicle motion and

https://doi.org/10.5194/egusphere-2026-2441
Preprint. Discussion started: 2 July 2026

attitude variations on wind measurements are explicitly accounted for, enabling a unified correction algorithm of vehicle-mounted instantaneous wind measurements under different inflow wind directions. To evaluate the performance of the proposed correction scheme, validation experiments were conducted in which the corrected wind data from vehicle-mounted measurements were pair-compared with concurrent and collocated wind data from ground-based anemometer observations. From such CFD-derived parameterization and validation, the correction algorithm provides a practical and efficient application to vehicle-mounted wind measurements, addressing the needs for near-surface wind vector data for meteorological modelling and forecasting under complex flow environments.

2 Methods

2.1 Vehicle geometry and digital model construction

The mobile atmospheric observation platform used in this study was developed based on a light-duty cargo-van, a JMC Ford Transit (Fig. 1a). A high-frequency three-dimensional ultrasonic anemometer (CSAT3B, Campbell Scientific, USA) was mounted on the vehicle roof. The instrument provides 3-d wind velocity components along the longitudinal, lateral, and vertical directions of the vehicle at sampling frequencies up to 20 Hz. It has a measurement accuracy of 0.001 m s^{-1} and a range of 0–65 m s^{-1}, suitable for capturing instantaneous wind velocities and turbulent flow characteristics. The CSAT3B also provides pitch and roll angle data at a frequency of 1 Hz with an accuracy of 1°, which are used to support the analysis of vehicle attitude dynamics. To obtain vehicle position and heading information during operation, the platform was equipped with a BeiDou GNSS-based real-time kinematics (RTK)-capable positioning system (BT-641B, Beitian Communication, China). Operating in differential mode, the system achieves centimetre-level positioning accuracy and outputs vehicle position, speed, and heading at a frequency of 2 Hz. In addition, the system was equipped with a high-precision digital compass (KVH-C100, KVH Inc., USA), which provides redundant heading measurements at a frequency of 1 Hz. This sensor offers a more stable and accurate reference for vehicle heading during acceleration, deceleration, and small steering manoeuvres.

https://doi.org/10.5194/egusphere-2026-2441
Preprint. Discussion started: 2 July 2026

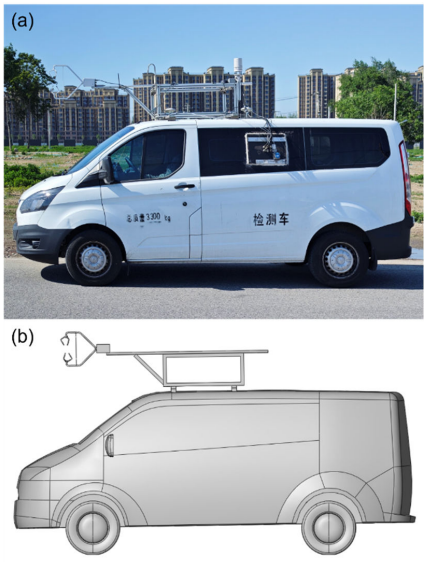

Figure 1: Schematic of the Peking University mobile atmospheric observation platform. (a) Photograph of the vehicle-mounted observation platform; (b) corresponding digital model.

Following the construction of the observation platform, a three-dimensional digital model of the vehicle was constructed to perform numerical simulations of vehicle-induced flow distortion under different wind speed and wind direction conditions (Fig. 1b). In this study, the vehicle was scanned from multiple viewing angles using a Zenmuse L2 LiDAR system mounted on a DJI M300 RTK UAV (DJI, China) (Fig. S1). The acquired high-density point cloud data of the vehicle exterior were pre-processed and subsequently wrapped into a polygonal mesh to generate a continuous surface representation of the vehicle geometry, which was further manually refined based on key vehicle dimensions obtained from direct measurements. Detailed features such as door handles, antennas, and small local protrusions were moderately simplified during the modelling process to avoid disproportionally large influences on the mesh generation., whereas key geometric features that play dominant roles in the vehicle aerodynamic behaviour, including the curvature of the vehicle front, the inclination of the windshield, and the roof mounted platform, were fully preserved. The digital model of the roof-mounted ultrasonic anemometer (CSAT3B) was provided by the manufacturer and integrated into the full vehicle model according to its actual dimensions.

To improve the CFD mesh quality and numerical stability, additional treatment was applied to the vehicle ground contact region at the final stage of geometry construction. Because the actual contact angle between the vehicle tyres and the ground is close to 0°, directly meshing this region can lead to severe cell distortion and, consequently, compromise the stability of flow field solutions. Therefore, a horizontal cutting plane was introduced at the bottom of the tyres, truncating them to form a regular geometry with a flat lower surface. As a result, the tyre ground contact region was represented as a truncated cone,

https://doi.org/10.5194/egusphere-2026-2441
Preprint. Discussion started: 2 July 2026

with an inclination angle of 45° between the conical surface and the base plane, and a height set to 2.5% of the tyre radius. This treatment effectively avoids mesh degradation in the contact region while preserving the aerodynamic realism of the vehicle underbody at the macroscopic scale (Leśniewicz et al., 2014). With the above optimizations, the resulting vehicle digital model (Fig. 1b) accurately reproduces the key geometric features of the vehicle while satisfying the quality requirements for CFD mesh generation, thereby providing a reliable basis for subsequent parameterized numerical simulations.

2.2 CFD parameterization and simulation setup

2.2.1 Computational domain and mesh configuration

Numerical simulations of the external flow field around the vehicle were performed using the Fluent simulation system. Fluent is based on a pressure coupled finite volume method and supports both steady and unsteady three-dimensional turbulent flow simulations. It is capable of handling complex geometries, unstructured meshes, and large computational domains, and has been widely applied in vehicle aerodynamics and environmental flow simulations (Broniszewski and Piechna, 2019; Kurec, 2022; Wu and Agarwal, 2023; Ramachandran et al., 2024). To accommodate the complex curved surfaces of the present vehicle geometry while maintaining overall mesh quality and sufficient resolution in key regions, an unstructured mesh composed of polyhedral cells was employed. This mesh strategy allows flexible placement of high-resolution cells in geometrically complex areas, such as the instrument mount, roof platform, and windshield, thereby enabling accurate simulation of the flow field. Unlike studies that focus on evaluating overall aerodynamic characteristics of vehicles, this study aims to quantify flow distortions at the location of the roof mounted anemometer to support the development of subsequent wind correction algorithm.

To ensure the physical integrity of the vehicle flow simulations and to minimize the influence of computational boundaries on the flow field structure, a hemispherical computational domain was adopted to solve the external flow around the vehicle (Fig. 2a). The vehicle dimensions are 4.973 m × 2.407 m × 2.766 m, and the domain radius was set to 25 m, corresponding to approximately 6–10 times the characteristic length scale of the vehicle. This configuration allows the incoming flow to develop sufficiently before reaching the vehicle and prevents the wake and recirculation regions from being affected by the domain boundaries. The hemispherical computational domain was selected for two main reasons. First, compared with conventional rectangular wind tunnel type domains, a hemispherical domain provides improved geometric isotropy, which reduces wall effects associated with the top and side boundaries and thereby minimises non-physical interference with the flow above and around the vehicle. Second, the hemispherical domain does not require adjustment of boundary configurations under different inflow wind directions, allowing a unified domain setup to be maintained. This feature is particularly suitable for the multi directional parameterized simulations required in this study and ensures consistency and repeatability across a large number of simulated cases. To ensure a consistent spatial reference for the vehicle external flow simulations, a Cartesian coordinate system was defined as follows: the x axis is oriented rearward along the vehicle, pointing from the front toward the rear; the y

https://doi.org/10.5194/egusphere-2026-2441
Preprint. Discussion started: 2 July 2026

axis is positive toward the left side when facing the vehicle front; and the *z* axis is defined as positive in the vertical upward direction.

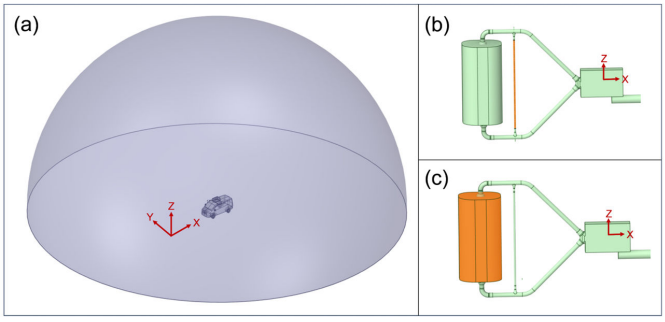

Figure 2: Schematic of the hemispherical computational domain and the locally refined boy of influence (BOI) for the vehicle-mounted platform. (a) External computational domain of the vehicle-mounted platform; (b) locally refined region BOI1; (c) locally refined region BOI2.

After the computational domain was defined, an unstructured mesh based on polyhedral cells was employed to better resolve local flow features near the vehicle surface and around the anemometer. Two locally refined regions, defined as bodies of influence (BOI), were introduced at the anemometer location, as illustrated in Fig. 2b and c. The target mesh sizes for BOI1 and BOI2 were set to 0.001 m and 0.0015 m, respectively, with a growth rate of 1.2 for both regions, in order to refine the local flow structures around the anemometer and its mounting structure. The surface mesh on the vehicle exterior was generated under curvature and proximity constraints, with a minimum face element size of 0.0015 m and a maximum size of 0.5 m. In addition, mesh variation on curved surfaces was controlled by limiting the curvature normal angle to 18°. After surface mesh generation, a uniform cell volume growth rate of 1.2 and a cell quality constraint of 0.35 were applied to the volume mesh to avoid the formation of highly skewed cells. No additional structured boundary layer mesh was constructed. Instead, mesh quality in key regions of the vehicle was ensured through the combined use of local mesh refinement and surface mesh controls. The resulting volume mesh consisted of approximately 4.2×10^6 cells. Details of the mesh configuration are shown in Fig. 3. The minimum orthogonal quality was 0.172, exceeding the commonly adopted threshold of 0.15, indicating that the overall mesh quality was sufficient to meet the convergence and accuracy requirements of vehicle flow simulations. A summary of the mesh parameters is provided in Table 1.

https://doi.org/10.5194/egusphere-2026-2441
Preprint. Discussion started: 2 July 2026

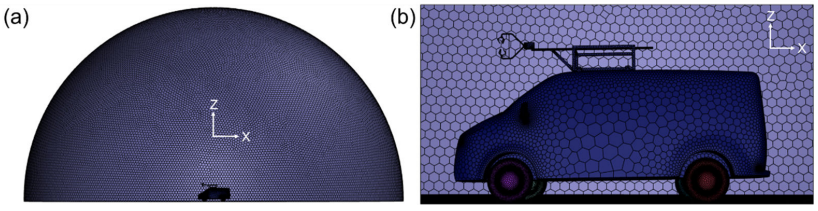

Figure 3: Mesh configuration of the computational domain and the vehicle-mounted platform. (a) Overall mesh distribution of the computational domain; (b) mesh distribution around the vehicle-mounted platform and its surrounding region.

Table 1: Key parameters for the computational domain and mesh generation.

Category	Parameter	Content
Computational domain	Domain type	Hemispherical
	Domain radius	25 m
	Platform dimensions	4.973 m × 2.407 m × 2.766 m
Local refinement regions (BOI)	BOI1 target mesh size	0.001 m
	BOI2 target mesh size	0.0015 m
	Size growth rate	1.2
Surface mesh	Minimum element size	0.0015 m
	Maximum element size	0.5 m
	Curvature control parameter	Curvature normal angle 18°; single layer curvature refinement
	Sizing method	Curvature and Proximity
Volume mesh	Mesh type	polyhedral
	Volume mesh growth rate	1.2
	Cell quality limit	0.35
Overall mesh assessment	Total cell count	4.2×10^6
	Minimum orthogonal quality	0.172

2.2.2 Solver settings and physical models

A pressure-based solver was employed to perform steady Reynolds averaged Navier–Stokes (RANS) simulations, and the SST k-ω turbulence model was adopted to resolve the external flow field around the vehicle. The SST k-ω model combines the characteristics of the k-ε and k-ω models, retaining the capability of the k-ω formulation to accurately capture boundary layer development and flow separation in near wall regions, while smoothly transitioning to the k-ε model in the free stream to achieve improved numerical stability (Menter et al., 2003). Air in the computational domain was treated as an ideal gas to account for variations in atmospheric density associated with changes in the flow state. The inlet boundary was specified as a

https://doi.org/10.5194/egusphere-2026-2441
Preprint. Discussion started: 2 July 2026

velocity inlet, which facilitates the subsequent parameterization procedure. Under low-speed external flow conditions, this configuration allows density variations induced by temperature and pressure to be considered, while ensuring proper pressure recovery and mass conservation near the outlet boundary. The vehicle surface and the ground were both defined as no slip walls. Apart from these core settings, other turbulence related parameters, such as turbulence intensity and turbulence length scale, were kept at their default values in Fluent.

2.2.3 Parameterization scheme and model outputs

Before conducting the parameterized numerical simulations, it is necessary to clarify the physical meaning of the wind speed measured by the vehicle-mounted anemometer. The three-dimensional ultrasonic anemometer installed on the vehicle roof outputs instantaneous velocity components defined in its own coordinate system, which represent the relative wind associated with the local flow field under vehicle motion. In this study, when the coordinate system of the anemometer is aligned with that of the vehicle, the anemometer-measured wind vector in the vehicle coordinate system ($\boldsymbol{v}_{\mathrm{m}}$) can be expressed as the vector sum of the true relative wind vector ($\boldsymbol{v}_{\mathrm{r}}$) and the vehicle induced flow distortion ($\Delta\boldsymbol{v}$) (Belusic et al., 2014; Miller et al., 2019):

$$\boldsymbol{v}_{\mathrm{m}} = \boldsymbol{v}_{\mathrm{r}} + \Delta\boldsymbol{v}. \quad (1)$$

where $\boldsymbol{v}_{\mathrm{m}}$ reflects the combined effects of the ambient wind, vehicle motion, and vehicle induced flow distortion. $\boldsymbol{v}_{\mathrm{r}}$ represents the true relative wind vector and is the target quantity to be retrieved; $\boldsymbol{\Delta v}$ denotes the velocity offset induced by the vehicle geometry, disturbances caused by vehicle attitudes, and the associated disturbed flow field. The objective of this study is to establish a mapping between $\boldsymbol{v}_{\mathrm{m}}$ and $\boldsymbol{v}_{\mathrm{r}}$ through CFD parameterized simulations to determine $\boldsymbol{\Delta v}$.

The true relative wind vector ($\boldsymbol{v}_{\mathrm{r}}$) is related to the true ambient wind vector ($\boldsymbol{v}_{\mathrm{e}}$) as follows

$$\boldsymbol{v}_{\mathrm{e}} = \boldsymbol{v}_{\mathrm{r}} - \boldsymbol{v}_{\mathrm{veh}} = \boldsymbol{v}_{\mathrm{m}} - \Delta\boldsymbol{v} - \boldsymbol{v}_{\mathrm{veh}}. \quad (2)$$

where $\boldsymbol{v}_{\mathrm{veh}}$ denotes the vehicle motion velocity vector. The objective of this study is to determine $\boldsymbol{\Delta v}$, and to ultimately solve for $\boldsymbol{v}_{\mathrm{e}}$ from $\boldsymbol{v}_{\mathrm{m}}$ and $\boldsymbol{v}_{\mathrm{veh}}$, thereby enabling the reconstruction and correction of the true ambient wind.

To establish the mapping between $\boldsymbol{v}_{\mathrm{m}}$ and $\boldsymbol{v}_{\mathrm{r}}$ and hence determine the correction term $\boldsymbol{\Delta v}$, a large number of CFD simulations must be conducted under multiple wind speed and direction conditions. Repeating the solver setup for each individual case would be highly time consuming and inefficient. The ANSYS Workbench provides a parameterization framework that allows key simulation variables to be defined as parameters while keeping the model structure unchanged, thereby enabling the establishment of the mapping between input and output parameters. Using this approach, batch simulations under multiple flow conditions can be efficiently performed within a unified solver setup by updating parameter values. In this study, the three-dimensional components of the true ambient wind velocities (representing the relative inflow wind) were defined as input parameters, while the three-dimensional wind velocity components in the vicinity of the anemometer were specified as output parameters. This parameterized simulation strategy substantially improves the computational efficiency required for large scale multi case simulations.

https://doi.org/10.5194/egusphere-2026-2441
Preprint. Discussion started: 2 July 2026

It should be noted that, in the numerical simulations, the vehicle is set as stationary ($v_{\mathrm{veh}} = 0$). Under this condition, the true relative inflow wind vector used in the CFD simulations ($\boldsymbol{v}_{\mathrm{r}}$) is equivalent to the true ambient wind vector ($\boldsymbol{v}_{\mathrm{e}}$) as per Eq (2), hence $\boldsymbol{v}_{\mathrm{r}} = \boldsymbol{v}_{\mathrm{e}}$. However, to maintain physical consistency in the model formulation, $\boldsymbol{v}_{\mathrm{r}}$ is used to denote the inflow wind vector in the CFD simulations, whereas $\boldsymbol{v}_{\mathrm{e}}$ is used in the wind correction procedure to represent the true ambient wind vector to be retrieved. In the simulation, the input parameters in the CFD simulations include only the two horizontal components of the ambient wind, namely $v_{\mathrm{r}x}$ and $v_{\mathrm{r}y}$, based on the fact that vertical wind velocities are generally small. Indeed, previous studies have similarly assumed time-averaged vertical wind component to be approximately zero (Belusic et al., 2014; Miller et al., 2019). In addition, after hybrid initialization of each simulation case, a cubic control volume with a side length of 3 cm was defined, centred at the geometric centre of the anemometer (Fig. S2). The mean wind velocity components in the x-, y-, and z-directions within this control volume, denoted as $v_{\mathrm{m}x}$, $v_{\mathrm{m}y}$ and $v_{\mathrm{m}z}$, respectively, were extracted and used as output parameters.

As the vehicle-mounted platform is symmetric about its longitudinal centreline (the y axis), only scenarios for inflow wind directions from half side are required to cover the full range of wind directions, and the results are the mirror-image for the other half side. Within the computational domain, the vehicle remains stationary, and the inlet wind velocity therefore represents the relative inflow wind. Considering the typical driving speed during mobile measurements, particularly for urban settings, at 20–30 km h^{-1} and the fact that ambient wind speeds are generally lower than 5 m s^{-1}, scenarios consisting of combinations of inflow wind speed and inflow angle were prescribed to compute the horizontal wind components $v_{\mathrm{r}x}$ and $v_{\mathrm{r}y}$ (Fig. 4). The inflow angle α is defined as the angle between the ambient wind direction and the forward direction of the vehicle (positive x axis), with positive values measured clockwise. Here, $\alpha = 0°$ corresponds to a pure headwind, while $\alpha = 180°$ represents a pure tailwind. The inflow α angle was varied from 0° to 180° with 5° increments. The wind speed was set to 0, 1, 2, 3, 4, 5, 10, 15, 20, 25, 30, 35, and 40 km h^{-1}, resulting in a total of 481 simulation scenarios. The cases with zero wind speed were included to ensure numerical stability. After removing duplicate configurations, a total of 445 independent simulation cases were retained. To ensure numerical stability and solution accuracy, the residuals of the velocity components in the x-, y-, and z-directions, continuity, energy, turbulent kinetic energy (k), and specific dissipation rate (ω) were monitored as convergence criteria and simultaneously recorded as output parameters during the iterative process. Each simulation was iterated for 100–300 iterations, and only solutions with all monitored residuals below 10^{-3} were retained (Houston et al., 2016).

Results from these simulations were grouped to obtain the correction algorithm, i.e., the relationship between $\Delta\boldsymbol{v}$ and $\boldsymbol{v}_{\mathrm{r}}$ under each simulation scenario and to determine how the inflow angles α and wind speeds $\boldsymbol{v}_{\mathrm{r}}$ influences this relationship. In other words, these two parameters are used to predict $\Delta\boldsymbol{v}$.

https://doi.org/10.5194/egusphere-2026-2441
Preprint. Discussion started: 2 July 2026

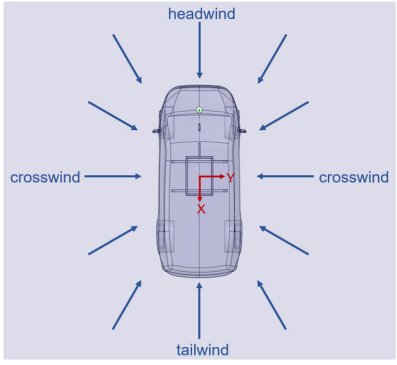

Figure 4: Schematic illustration of different inflow wind directions relative to the vehicle-mounted platform.

2.3 Field validation experiment for three-dimensional wind velocity correction

To validate the performance of the wind correction algorithm, a field comparison experiment was conducted in a vacant area where a public east-west road of about 300 m runs through. The site is characterised by flat terrain, minimal surrounding vegetation, and the absence of buildings within 200 meters, with a very low traffic volume. These conditions provide an open and unobstructed environment, thereby minimizing external environmental interference during the measurements. A temporary ground-based wind observation system was deployed approximately 3 m north of the road (Fig. 5a), equipped with the same CSAT3B three-dimensional ultrasonic anemometer as that mounted on the vehicle. The ground-based anemometer was installed at the same height as the vehicle-mounted anemometer at 2.5 m above ground level. The ground-based wind velocity measurement was recorded at a frequency of 1 Hz, while pitch and roll angles were output at 5 Hz, ensuring the measurement comparability between the ground-based and vehicle-mounted systems.

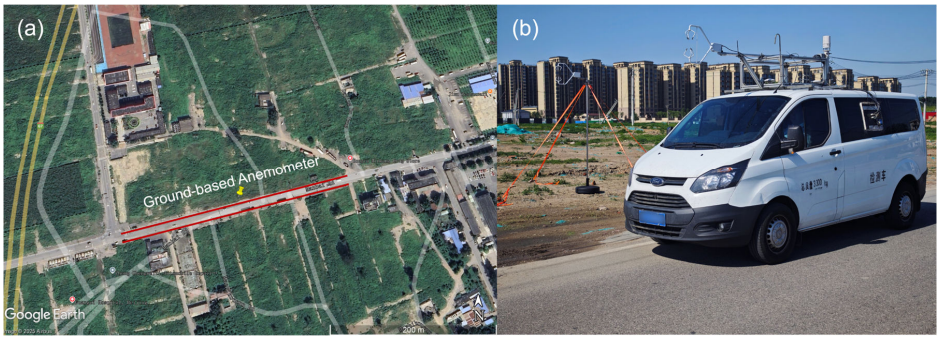

Figure 5: Field validation site and deployment of the ground-based anemometer. (a) Satellite image of the validation site, where the yellow marker indicates the location of the ground-based anemometer and the red lines denote the vehicle driving trajectories

https://doi.org/10.5194/egusphere-2026-2441
Preprint. Discussion started: 2 July 2026

in both directions; (b) field deployment and synchronous observations of the vehicle-mounted platform and the ground-based anemometer. The satellite image in panel (a) is from Google Earth. Map data © Google, Airbus.

The field experiments were conducted on six days under clear skies and moderate wind conditions between 13 and 21 May 2025. The ground-based anemometer was oriented to align with the road direction and was set to face west. Its heading angle was recorded using a GPS to facilitate consistent data processing across different measurement systems. During the experiments, the vehicle was driven back and forth along the red trajectories shown in Fig. 5a, with driving speeds controlled at 5, 10, 15, 20, 25, 30, 35, and 40 km h^{-1}. Each driving speed was maintained for 20–40 min. Depending on the prevailing wind conditions on a given day, the field experiment may have covered all speed levels or only a subset of them, ensuring that sufficient data samples were obtained under different relative wind speed conditions. Table S1 summarises the data acquisition details for each experimental day. In total, approximately 16 h of valid mobile and ground-based wind measurements were obtained.

3 Results and discussion

3.1 Characteristics of the external flow field under typical scenarios

As aforementioned, a parameterized simulation ensemble was constructed by combining different inflow angles ($\alpha = 0 - 180°, \Delta\alpha = 5°$) and wind speeds (0–40 km h^{-1}) resulting in a total of 445 independent CFD simulation cases. To provide an intuitive illustration of the flow field characteristics around the vehicle-mounted platform under different ambient wind conditions, and to quantify the velocity disturbances at the anemometer sensor position, two sets of comparative analyses were designed. The first set focuses on the influence of inflow wind speed on the vehicle induced flow field, while the second set examines the flow field differences arising from variations in inflow wind direction.

In the first set of numerical experiments, a pure headwind condition ($\alpha = 0°$) was selected as a representative scenario to investigate the influence of inflow wind speed on the external flow field around the vehicle-mounted platform. Figure 6 first presents the cross-sectional views of the velocity magnitude around the vehicle for an inflow wind speed of 10 km h^{-1} (2.78 m s^{-1}), where the colour scale indicates the wind speed magnitude. Under headwind conditions, a characteristic upstream deceleration region develops in front of the vehicle (Fig. 6a), with the local wind speed decreasing rapidly from the free stream value of 2.78 m s^{-1} to below 1 m s^{-1}. After the flow passes the vehicle front, it continues to be influenced by geometric blockage and pressure buildup along the vehicle roof. As a result, the local wind speed remains below the free stream level. In the vicinity of the anemometer sensor, no distinct acceleration zone is observed. The flow is characterised primarily by decelerated boundary layer behaviour. The x component of the wind velocity (Fig. 6b) further illustrates the spatial distribution of acceleration and deceleration. A pronounced negative region appears upstream of the vehicle, indicating substantial deceleration of the incoming flow caused by blockage at the vehicle front. After the flow bypasses the vehicle hood, the x component of the flow in the vicinity of the anemometer installation remains lower than the free stream value, indicating that

https://doi.org/10.5194/egusphere-2026-2441
Preprint. Discussion started: 2 July 2026

the local flow is still in a decelerated state. As the flow continues to develop downstream along the vehicle roof, streamline contraction leads to local acceleration, forming an acceleration band with x velocity components slightly exceeding the free stream value over the mid to rear section of the roof. After passing the vehicle rear, flow separation occurs and generates an extended low speed wake region downstream of the vehicle. The z component of the wind velocity around the vehicle (Fig. 6c) reveals the presence of upward and downward motion under headwind conditions. A pronounced upward flow is observed above the vehicle front, while a weak downward motion appears beneath the vehicle body. Overall, the flow distortion in the vicinity of the anemometer sensor, although apparent, remains relatively limited under headwind conditions and is mainly associated with the development of the roof boundary layer. These flow characteristics are consistent with previous findings reported by Houston (2016) and Hanlon and Risk (2020).

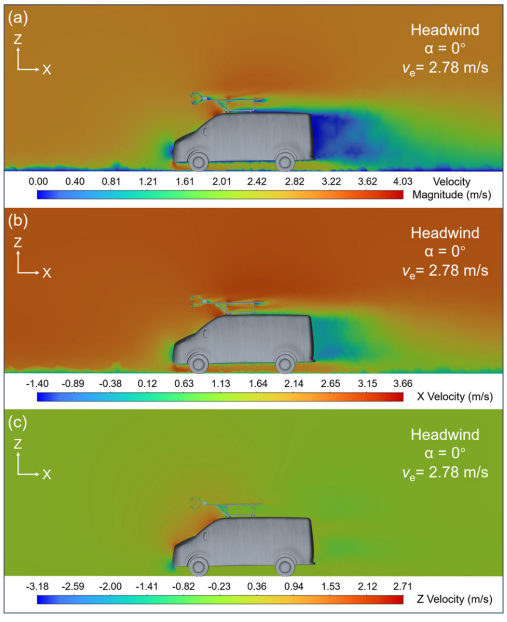

Figure 6: Example CFD simulation results of the flow field around the vehicle-mounted platform under pure headwind conditions ($\alpha = 0°$, inflow wind speed of 2.78 m s^{-1}). (a) Velocity magnitude; (b) x component of the wind velocity; (c) z component of the wind velocity.

The inflow wind speed was variously set to 5, 20, and 40 km h^{-1} (1.39, 5.55, and 11.11 m s^{-1}) in further simulations, and the corresponding results are separately shown in Fig. 7a–c, respectively. From an overall perspective, the structure of the velocity field around the vehicle remains consistent as the inflow wind speed varies. The main flow features, including the upstream

https://doi.org/10.5194/egusphere-2026-2441
Preprint. Discussion started: 2 July 2026

deceleration region, the moderately decelerated flow in the vicinity of the anemometer assembly, and the low-speed wake downstream of the vehicle, are preserved across all cases. No fundamental changes in the flow pattern are observed. These results indicate that, under headwind conditions, the vehicle induced flow structure exhibits a pronounced degree of scale similarity. Variations in inflow wind speed primarily lead to changes in velocity gradients rather than fundamental alterations of the flow pattern. On the other hand, although the overall flow structure remains stable, the velocity magnitude within different regions shows clear differences among the cases. At lower inflow wind speed (Fig. 7a), the upstream deceleration region is relatively limited in extent, and the flow deceleration at the anemometer sensor location is comparatively weak. When the inflow wind speed increases to 5.55 m s^{-1} (Fig. 7b) and above (Fig. 7c), the velocity decreases within both the upstream deceleration region and the downstream wake become substantially stronger. Meanwhile, over the mid to rear section of the vehicle roof downstream of the anemometer, a local acceleration band develops. The peak velocity within this band increases markedly with increasing free stream wind speed. This behaviour reflects the strengthening of streamline contraction as the inflow wind speed increases. It should be noted that the anemometer sensor location consistently remains within a locally decelerated region. While the local wind speed at this position increases approximately linearly with the free stream wind speed, the spatial distribution of the flow distortion remains largely unchanged. This indicates that, under headwind conditions, the flow distortion in the vicinity of the anemometer sensor is primarily governed by the geometry of the vehicle-mounted platform and the anemometer installation. Variations in the free stream wind speed mainly affect the magnitude of the disturbance, while having a limited influence on its spatial structure.

https://doi.org/10.5194/egusphere-2026-2441
Preprint. Discussion started: 2 July 2026

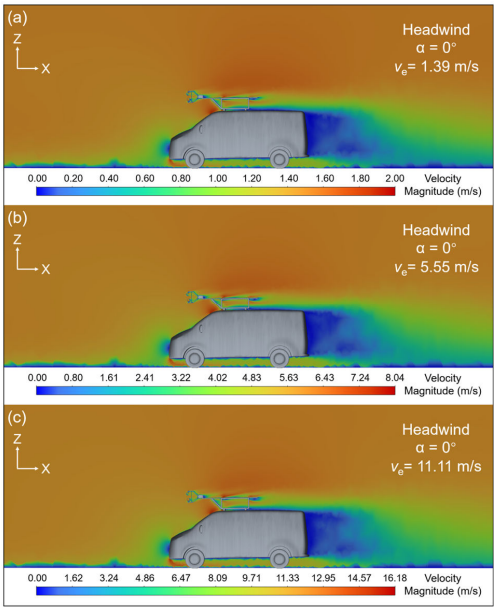

Figure 7: Example CFD simulation results of the flow field around the vehicle-mounted platform under pure headwind conditions ($\alpha = 0°$) at different inflow wind speeds. Panels (a)–(c) correspond to inflow wind speeds of 1.39, 5.55, and 11.11 m s^{-1}, respectively.

To investigate the flow field differences induced by variations in the inflow wind direction, the second set of experiments examines five representative wind direction scenarios, including pure headwind, pure tailwind, crosswind, and two oblique inflow conditions at angles of 45° and 135°. For ease of comparison among different wind directions, the inflow wind speed was fixed at a representative relative velocity of 10 km h^{-1} (2.78 m s^{-1}). Figures 7a and 8a–f present cross-sectional distributions of the velocity field around the vehicle-mounted platform under the five wind direction scenarios described above. In contrast to the first set of experiments (Fig. 7), pronounced differences in the flow field structure are observed when the inflow wind direction varies. Changes in the wind direction not only shift windward surface locations and the primary flow paths around the vehicle, but also lead to substantial variations in flow separation, local acceleration, and wake structures over different parts of the vehicle. As a result, the characteristics of the local flow distortion at the anemometer sensor location become considerably more sensitive to wind direction. Figures 7a and 8a–f present cross-sectional distributions of the velocity field around the vehicle-mounted platform under the five wind direction scenarios described above. In contrast to the first set of experiments, pronounced differences in the flow field structure are observed when the inflow wind direction varies.

https://doi.org/10.5194/egusphere-2026-2441
Preprint. Discussion started: 2 July 2026

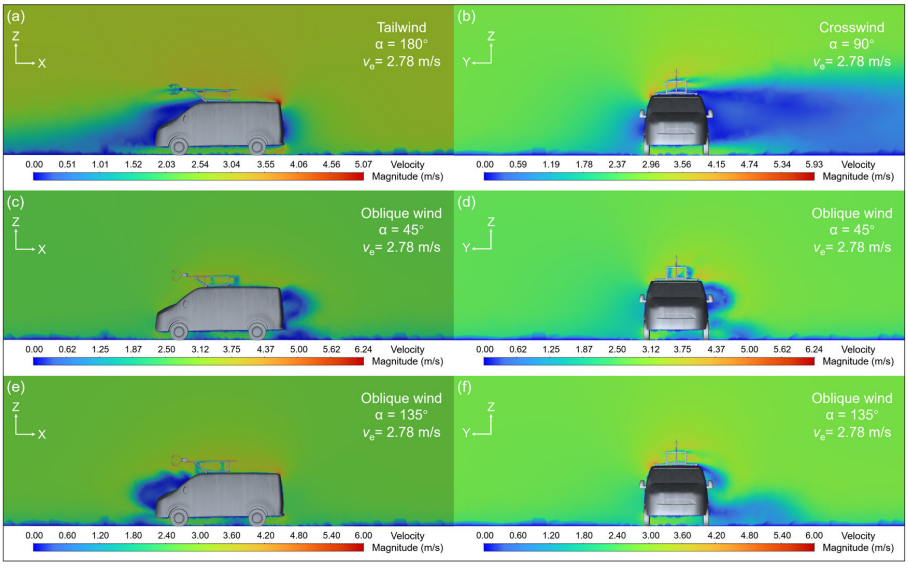

Figure 8: Example CFD simulation results of the flow field around the vehicle-mounted platform under different inflow wind directions at an inflow wind speed of 2.78 m s^{-1}. (a) Pure tailwind ($\alpha = 180°$); (b) crosswind ($\alpha = 90°$); (c) side view and (d) front view under oblique inflow conditions with $\alpha = 45°$; (e) side view and (f) front view under oblique inflow conditions with $\alpha = 135°$.

Under pure tailwind conditions ($\alpha = 180°$), the incoming flow first interacts with the box shaped housing at the rear of the vehicle roof and the anemometer mounting structure. This interaction generates a strong wake and produces a pronounced low speed region in the vicinity of the probe (Fig. 8a). In this configuration, the anemometer mounting structure exerts a dominant influence on the local flow field, placing the anemometer sensor directly within the wake. Compared with the headwind condition, the flow field undergoes a fundamental change and exhibits a characteristic wake dominated disturbance structure. Overall, the local inflow wind speed at the anemometer location is reduced by more than 50% relative to the free stream value of 2.78 m s^{-1}, demonstrating the pronounced impact of tailwind conditions on wind speed measurements.

Under crosswind conditions ($\alpha = 90°$), the flow field around the vehicle-mounted platform exhibits pronounced asymmetry (Fig. 8b). Unlike the longitudinally symmetric flow patterns observed under headwind and tailwind conditions, lateral inflow causes substantial differences between the windward and leeward sides of the vehicle. This leads to a lateral displacement of the primary flow paths, shifts in the locations of flow separation, and the development of non-uniform lateral velocity gradients. On the windward side of the vehicle, the incoming flow forms a high-pressure region and is accelerated upward along the vehicle surface. On the leeward side, an extended low speed region develops together with a more complex wake structure. Overall, the measurement bias at the anemometer sensor location under crosswind conditions mainly arises from flow

https://doi.org/10.5194/egusphere-2026-2441
Preprint. Discussion started: 2 July 2026

asymmetry and the development of lateral shear layers. The disturbance intensity lies between that observed under tailwind and headwind conditions, while the flow structure is noticeably more complex.

Under oblique inflow conditions ($\alpha = 45°$ and $\alpha = 135°$), the flow structure exhibits a combined behaviour characterised by headwind or tailwind features together with lateral deflections (Fig. 8c–f). The $\alpha = 45°$ case more closely resembles a headwind dominated structure, with the flow around the probe primarily influenced by upstream acceleration and flow direction deflection. In contrast, the $\alpha = 135°$ case is dominated by a tailwind component, leading to a more pronounced velocity reduction at the sensor location. The additional lateral component causes the wake structure to shift and become distorted. Taken together, inflow wind speed and wind direction predominantly control both the magnitude and spatial structure of the flow distortion. Both factors jointly constitute the primary sources of the velocity offset $\boldsymbol{\Delta v}$ in Eq. (1). This further demonstrates the necessity of conducting parameterized CFD simulations across a wide range of wind speeds and wind directions.

3.2 Flow features under headwind and tailwind conditions

In practical mobile measurements, the distribution of ambient wind directions relative to the vehicle-mounted platform is not uniform. Different relative wind direction conditions differ substantially in both their occurrence frequency and associated disturbance mechanisms. For the purpose of analysis and modelling, the relative wind direction was classified into two major categories based on the vehicle coordinate system, with the x axis defined as the vehicle forward direction. The first category is referred to as the headwind condition, in which the relative inflow wind angle α atisfies $-90° \leq \alpha \leq 90°$. The second category is referred to as the tailwind condition, corresponding to $90° \leq \alpha \leq 270°$ ($\mathrm{i.e.}, -90°$). In terms of occurrence frequency, the majority of mobile measurement samples fall within headwind conditions due to the forward vehicle motion during driving, while tailwind conditions occur less frequently, only under situations where the forward component of the wind vector along the x-axis exceeds the vehicle driving speed. However, tailwind conditions may still arise when the vehicle speed is relatively low and the ambient wind speed is comparatively high. Such situations are more commonly encountered in mobile measurements conducted around small scale targets such as oil and natural gas production and transport facilities (Brantley et al., 2014; Zhou et al., 2021), where low vehicle speeds are often necessary.

From a physical perspective, flow distortion at the anemometer sensor under headwind conditions is primarily governed by the flow around the vehicle front and the development of the roof boundary layer. As the inflow wind strength varies, the resulting distortion exhibits a relatively stable and near linear response. In contrast, flow distortion at the sensor under tailwind conditions is dominated by the recirculation region behind the vehicle and the wake generated by the anemometer mounting structure, leading to stronger nonlinearity and increased unsteadiness in the anemometer sensor output. It is worth noting that wind measurement biases induced under tailwind conditions are generally more pronounced. This distinction provides the primary basis for constructing separate correction models for headwind and tailwind conditions in the subsequent algorithm development. In addition, owing to the left–right symmetry of the vehicle-mounted platform with respect to its longitudinal centreline (y axis), the parameterized CFD simulations were conducted only for inflow wind directions within the range of 0–

https://doi.org/10.5194/egusphere-2026-2441
Preprint. Discussion started: 2 July 2026

180°. Conditions with $\alpha < 0°$ and $\alpha > 180°$can be mapped to the corresponding cases within 0–90° and 90–180° through symmetry considerations. In this section, no mirroring or symmetry-based data augmentation is applied. The quantitative analysis focuses solely on the relationship between the relative wind vector $\boldsymbol{v}_{\mathrm{r}}$ and the flow-distorted wind vector $\boldsymbol{v}_{\mathrm{m}}$ measured by the anemometer, based on the original CFD simulation results for the two wind direction conditions. Symmetry based data augmentation is introduced later during the algorithm construction in Section 3.3, where it is used to increase the size of the training dataset.

According to the definitions in Section 2.2.3, for each relative inflow wind vector $(v_{\mathrm{r}x}, v_{\mathrm{r}y}, v_{\mathrm{r}z})$, the corresponding flow-distorted wind vector measured at the anemometer sensor $(v_{\mathrm{m}x}, v_{\mathrm{m}y}, v_{\mathrm{m}z})$ can be obtained, as expressed in Eqs. (1) and (2). Because the vertical component of the ambient wind is typically small in the atmosphere, $v_{\mathrm{r}z}$ is set to zero in the present analysis, but for subsequent model construction, the vertical wind speed increment Δv_z is further defined. In the present CFD analysis, because $v_{\mathrm{r}z} = 0$, the measured vertical velocity component $v_{\mathrm{m}z}$ directly corresponds to this increment.

$$\Delta v_z = v_{\mathrm{m}z} - v_{\mathrm{r}z}. \tag{3}$$

To examine the most basic linear response characteristics of the flow distortion, $v_{\mathrm{m}x}$, $v_{\mathrm{m}y}$, and Δv_z are separately regressed against the inflow wind components $v_{\mathrm{r}x}$ and $v_{\mathrm{r}y}$ using bivariate linear models of the form

$$\hat{q} = a v_{\mathrm{r}x} + b v_{\mathrm{r}y} + c, \tag{4}$$

where q represents $v_{\mathrm{m}x}$, $v_{\mathrm{m}y}$, or Δv_z and $\hat{q}$ is the corresponding regression-based prediction. The detailed regression equations and performance statistics are provided in Sect. S3 of the Supplement.

Figures S3 and S4 compare the regression-based predictions with the corresponding CFD simulation results under headwind and tailwind conditions, respectively. Under headwind conditions, the three response variables show close agreement with the fitted linear models, indicating that the associated flow distortion is relatively stable and near-linear. By contrast, the fitting performance under tailwind conditions deteriorates markedly, especially for Δv_z, which exhibits a much larger scatter and lower goodness of fit. These results indicate that the flow distortion under headwind conditions is governed by a relatively simple linear response, whereas under tailwind conditions it is dominated by stronger wake-induced nonlinearity. This distinction provides the basis for constructing separate correction algorithm for headwind and tailwind conditions in Sect. 3.3.

3.3 Three-dimensional wind velocity correction methodology

In practical mobile measurements, the three-dimensional ultrasonic anemometer mounted on the vehicle outputs wind velocity components expressed in the vehicle coordinate system. These measurements are influenced by multiple factors, including flow distortions induced by the vehicle-mounted platform, the vehicle motion, and variations in vehicle attitude during driving. Therefore, to recover the true ambient wind velocity, a unified correction framework is required, in which these effects are represented by the flow distortion term ($\Delta \boldsymbol{V}_{\mathrm{D}}$), the attitude motion term ($\Delta \boldsymbol{V}_{\mathrm{A}}$), and the vehicle translation term ($\Delta \boldsymbol{V}_{\mathrm{V}}$). The term $\Delta \boldsymbol{V}_{\mathrm{D}}$ characterizes the local flow distortion caused by the interaction between the vehicle body and the incoming flow, and is corrected using a model derived from parameterized CFD simulations. The term $\Delta \boldsymbol{V}_{\mathrm{A}}$ accounts for the additional velocity

https://doi.org/10.5194/egusphere-2026-2441
Preprint. Discussion started: 2 July 2026

induced by variations in vehicle attitude and is determined from the roll, pitch, and yaw data. The term $\Delta \boldsymbol{V}_{\mathrm{V}}$ represents the contribution of vehicle translation to the measured wind velocity. This component must be removed in mobile measurements and is estimated from the time-differentials of vehicle positioning data obtained from the BeiDou-based positioning system. Accordingly, in the vehicle coordinate system, the corrected ambient wind velocity can be expressed as

$$\boldsymbol{v}_{\mathrm{e}} = \boldsymbol{v}_{\mathrm{m}} - \Delta \boldsymbol{V}_{\mathrm{A}} - \Delta \boldsymbol{V}_{\mathrm{D}} - \Delta \boldsymbol{V}_{\mathrm{V}}. \tag{5}$$

After these corrections, the wind velocity is transformed from the vehicle coordinate system into the standard geographic coordinate system through coordinate transformation, yielding the true ambient wind field.

3.3.1 CFD-based correction of vehicle-induced flow distortion

We first examine the effect of the flow distortion term $\Delta \boldsymbol{V}_{\mathrm{D}}$, which represents the aerodynamic disturbance induced by the vehicle body and forms the basis of the CFD-based correction algorithm. Given that the vehicle-mounted platform is symmetric with respect to its longitudinal centreline (the y axis), this geometric symmetry can be exploited to extend the original CFD dataset through symmetry mapping. Specifically, for each inflow wind velocity vector $(v_{\mathrm{r}x}, v_{\mathrm{r}y}, v_{\mathrm{r}z})$ and the corresponding flow distorted wind velocity measured at the anemometer location $(v_{\mathrm{m}x}, v_{\mathrm{m}y}, v_{\mathrm{m}z})$, an equivalent scenario can be obtained by applying a mirror transformation about the y axis, yielding an inflow wind vector $(v_{\mathrm{r}x}, -v_{\mathrm{r}y}, v_{\mathrm{r}z})$, and the corresponding distorted wind vector $(v_{\mathrm{m}x}, -v_{\mathrm{m}y}, v_{\mathrm{m}z})$. After applying this symmetry-based data augmentation to all simulated cases, a total of 457 independent scenarios were obtained for both headwind and tailwind conditions, respectively. These extended datasets were subsequently used for regression modelling and the development of the flow distortion correction algorithms.

To express vehicle-induced flow distortion in a form consistent with the unified correction algorithm, the flow distortion term $\Delta \boldsymbol{V}_{\mathrm{D}}$ is decomposed into three component-wise increments in the vehicle coordinate system:

$$\Delta \boldsymbol{V}_{\mathrm{D}} = \begin{bmatrix} \Delta v_x \\ \Delta v_y \\ \Delta v_z \end{bmatrix}, \tag{6}$$

$$\Delta v_x = v_{\mathrm{m}x} - v_{\mathrm{r}x}, \tag{7}$$

$$\Delta v_y = v_{\mathrm{m}y} - v_{\mathrm{r}y}, \tag{8}$$

$$\Delta v_z = v_{\mathrm{m}z} - v_{\mathrm{r}z}, \tag{9}$$

where Δv_x, Δv_y, and Δv_z denote the distortion-induced velocity increments in the x-, y-, and z-directions, respectively. These increments are defined as the differences between the flow-distorted wind velocity measured at the anemometer location and the corresponding true relative inflow velocity in the CFD simulations. Because the preliminary analysis in Sect. 3.2 showed distinct characteristics under headwind and tailwind conditions, separate correction algorithms are constructed for the two flow regimes. Accordingly,

$$\Delta \boldsymbol{V}_{\mathrm{D}}^{\mathrm{HW}} = \begin{bmatrix} \Delta v_x^{\mathrm{HW}} \\ \Delta v_y^{\mathrm{HW}} \\ \Delta v_z^{\mathrm{HW}} \end{bmatrix}, \tag{10}$$

https://doi.org/10.5194/egusphere-2026-2441
Preprint. Discussion started: 2 July 2026

$$\Delta \boldsymbol{V}_{\mathrm{D}}^{\mathrm{TW}} = \begin{bmatrix} \Delta v_x^{\mathrm{TW}} \\ \Delta v_y^{\mathrm{TW}} \\ \Delta v_z^{\mathrm{TW}} \end{bmatrix}, \tag{11}$$

where the superscript HW denotes headwind conditions. Similarly, TW is used for tailwind conditions, following the notation by Yang et al. (2025).

With these definitions, the final flow distortion correction algorithm is written in the unified form:

$$\boldsymbol{v}_{\mathrm{r}} = \boldsymbol{v}_{\mathrm{m}} - \Delta \boldsymbol{V}_{\mathrm{D}}, \tag{12}$$

where $\Delta \boldsymbol{V}_{\mathrm{D}}$ is specified as $\Delta \boldsymbol{V}_{\mathrm{D}}^{\mathrm{HW}}$ or $\Delta \boldsymbol{V}_{\mathrm{D}}^{\mathrm{TW}}$ for headwind and tailwind conditions, respectively.

For headwind conditions ($-90^\circ \le \alpha \le 90^\circ$), the flow distortion around the vehicle shows relatively stable linear characteristics. Based on the symmetry-extended CFD dataset, bivariate linear regression relationships are established with $v_{\mathrm{m}x}^{\mathrm{HW}}$, $v_{\mathrm{m}y}^{\mathrm{HW}}$, and Δv_z^{HW} as the dependent variables and the inflow wind components $v_{\mathrm{r}x}^{\mathrm{HW}}$ and $v_{\mathrm{r}y}^{\mathrm{HW}}$ as the independent variables. This yields Eqs. (13)–(15):

$$v_{\mathrm{m}x}^{\mathrm{HW}} = 0.97\, v_{\mathrm{r}x}^{\mathrm{HW}} - 0.18, \tag{13}$$

$$v_{\mathrm{m}y}^{\mathrm{HW}} = 1.15\, v_{\mathrm{r}y}^{\mathrm{HW}}, \tag{14}$$

$$\Delta v_z^{\mathrm{HW}} = 0.17\, v_{\mathrm{r}x}^{\mathrm{HW}} + 0.13. \tag{15}$$

Moreover, to maintain consistency with the unified disturbance-based correction algorithm adopted in this study, the above relations are further reformulated into disturbance expressions written in terms of the measured wind velocity components, as given in Eqs. (16)–(18). The detailed derivation is provided in Sect. S4 of the Supplement.

$$\Delta v_x^{\mathrm{HW}} = -0.01\, v_{\mathrm{m}x}^{\mathrm{HW}} - 0.18\, v_{\mathrm{m}z}^{\mathrm{HW}} - 0.15, \tag{16}$$

$$\Delta v_y^{\mathrm{HW}} = 0.13\, v_{\mathrm{m}y}^{\mathrm{HW}}, \tag{17}$$

$$\Delta v_z^{\mathrm{HW}} = 0.17\, v_{\mathrm{m}x}^{\mathrm{HW}} + 0.031\, v_{\mathrm{m}z}^{\mathrm{HW}} + 0.13. \tag{18}$$

Accordingly, the correction algorithm under headwind conditions can be written as

$$\begin{bmatrix} v_{\mathrm{r}x}^{\mathrm{HW}} \\ v_{\mathrm{r}y}^{\mathrm{HW}} \\ v_{\mathrm{r}z}^{\mathrm{HW}} \end{bmatrix} = \begin{bmatrix} v_{\mathrm{m}x}^{\mathrm{HW}} \\ v_{\mathrm{m}y}^{\mathrm{HW}} \\ v_{\mathrm{m}z}^{\mathrm{HW}} \end{bmatrix} - \begin{bmatrix} \Delta v_x^{\mathrm{HW}} \\ \Delta v_y^{\mathrm{HW}} \\ \Delta v_z^{\mathrm{HW}} \end{bmatrix}. \tag{19}$$

Under tailwind conditions ($90^\circ \le \alpha \le 270^\circ$), the inflow is primarily influenced by the combined effects of the vehicle rear geometry and the wake generated by the anemometer mounting structure. As a result, the associated flow distortion exhibits stronger nonlinearity and lower stability than that under headwind conditions, making it difficult to establish an effective inversion model using simple linear regression. A separate correction algorithm is therefore established for tailwind conditions. A mapping between the true relative wind direction $\beta_{\mathrm{r}}^{\mathrm{TW}}$ and the measured distorted wind direction $\beta_{\mathrm{m}}^{\mathrm{TW}}$ is first established based on the symmetry-extended CFD dataset. Here, $\beta_{\mathrm{r}}^{\mathrm{TW}}$ and $\beta_{\mathrm{m}}^{\mathrm{TW}}$ denote the true and measured relative wind directions in the vehicle coordinate system, respectively. The resulting quadratic relationship is given by

$$\beta_{\mathrm{r}}^{\mathrm{TW}} = -56.81 + 0.039\, \beta_{\mathrm{m}}^{\mathrm{TW}} - 0.0040\, (\beta_{\mathrm{m}}^{\mathrm{TW}})^2. \tag{20}$$

https://doi.org/10.5194/egusphere-2026-2441
Preprint. Discussion started: 2 July 2026

The three disturbance components under tailwind conditions are then parameterized as functions of the measured wind components and selected derived variables. In the following expressions, $V_{\mathrm{m}}^{\mathrm{TW}}$ denotes the measured horizontal wind speed magnitude. The detailed variable definitions and feature construction are provided in Sect. S5 of the Supplement. The final expressions for the tailwind disturbance components are

$$\Delta v_x^{\mathrm{TW}} \approx -0.28 + 3.42\,\left|v_{\mathrm{my}}^{\mathrm{TW}}\right| + 0.37\,(V_{\mathrm{m}}^{\mathrm{TW}})^2 + V_{\mathrm{m}}^{\mathrm{TW}}\left(-4.68 + 0.70\,v_{\mathrm{mx}}^{\mathrm{TW}} - 0.43\,\left|v_{\mathrm{my}}^{\mathrm{TW}}\right| - 0.046\,\beta_{\mathrm{r}}^{\mathrm{TW}}\right), \tag{21}$$

$$\Delta v_y^{\mathrm{TW}} = 0.095\,v_{\mathrm{my}}^{\mathrm{TW}} - 0.015\,v_{\mathrm{mx}}^{\mathrm{TW}} v_{\mathrm{my}}^{\mathrm{TW}}, \tag{22}$$

$$\Delta v_z^{\mathrm{TW}} \approx -0.11 + 2.04\,\left|v_{\mathrm{my}}^{\mathrm{TW}}\right| - 1.72\,v_{\mathrm{mx}}^{\mathrm{TW}} + V_{\mathrm{m}}^{\mathrm{TW}}(-2.43 + 0.13\,v_{\mathrm{mx}}^{\mathrm{TW}} - 0.018\,\beta_{\mathrm{r}}^{\mathrm{TW}}) + \beta_{\mathrm{r}}^{\mathrm{TW}}\left(-0.014\,v_{\mathrm{mx}}^{\mathrm{TW}} + 0.013\,\left|v_{\mathrm{my}}^{\mathrm{TW}}\right|\right). \tag{23}$$

Thus, under tailwind conditions, the true relative wind velocity can be obtained as

$$\begin{bmatrix} v_{\mathrm{rx}}^{\mathrm{TW}} \\ v_{\mathrm{ry}}^{\mathrm{TW}} \\ v_{\mathrm{rz}}^{\mathrm{TW}} \end{bmatrix} = \begin{bmatrix} v_{\mathrm{mx}}^{\mathrm{TW}} \\ v_{\mathrm{my}}^{\mathrm{TW}} \\ v_{\mathrm{mz}}^{\mathrm{TW}} \end{bmatrix} - \begin{bmatrix} \Delta v_x^{\mathrm{TW}} \\ \Delta v_y^{\mathrm{TW}} \\ \Delta v_z^{\mathrm{TW}} \end{bmatrix}. \tag{24}$$

3.3.2 Vehicle motion compensation, attitude compensation, and coordinate transformation

No analyses have been reported on the impacts on wind measurements of vehicle attitude changes during vehicle motion in reported wind correction schemes. During vehicle motion, the wind velocity measured by the vehicle-mounted anemometer represents the superposition of the true environmental wind velocity and the vehicle's own motion velocity (see Eq. (2)). Furthermore, when the vehicle rolls, bumps and turns, the attitude attributes roll (ϕ), pitch (θ) and yaw (or heading, ψ) angles change corresponding to rotations about the x-, y-, and z-axes of the vehicle coordinate system, respectively, thereby introducing additional signals at the anemometer sensor which need to be corrected for. Therefore, the final true three-dimensional environmental wind velocity components can be expressed by introducing the vehicle translation term $\Delta \boldsymbol{V}_{\mathrm{V}}$ and the attitude motion term $\Delta \boldsymbol{V}_{\mathrm{A}}$ as:

$$\begin{bmatrix} v_{ex} \\ v_{ey} \\ v_{ez} \end{bmatrix} = \begin{bmatrix} v_{\mathrm{rx}} \\ v_{\mathrm{ry}} \\ v_{\mathrm{rz}} \end{bmatrix} - \Delta \boldsymbol{V}_{\mathrm{V}} - \Delta \boldsymbol{V}_{\mathrm{A}}, \tag{25}$$

$$\Delta \boldsymbol{V}_{\mathrm{V}} = \begin{bmatrix} v_{\mathrm{veh}} \\ 0 \\ 0 \end{bmatrix}, \tag{26}$$

$$\Delta \boldsymbol{V}_{\mathrm{A}} = -\boldsymbol{\omega} \times \boldsymbol{r}, \tag{27}$$

$$\boldsymbol{\omega} = \begin{bmatrix} \omega_x \\ \omega_y \\ \omega_z \end{bmatrix} = \begin{bmatrix} \dot{\phi} \\ -\dot{\theta} \\ -\dot{\psi} \end{bmatrix}, \tag{28}$$

$$\boldsymbol{r} = \begin{bmatrix} r_x \\ r_y \\ r_z \end{bmatrix}, \tag{29}$$

https://doi.org/10.5194/egusphere-2026-2441
Preprint. Discussion started: 2 July 2026

$$\boldsymbol{\omega} \times \boldsymbol{r} = \begin{bmatrix} -\dot{\theta} r_z + \dot{\psi} r_y \\ -\dot{\psi} r_x - \dot{\phi} r_z \\ \dot{\phi} r_y + \dot{\theta} r_x \end{bmatrix}, \tag{30}$$

where v_{ex}, v_{ey}, and v_{ez} denote the true environmental wind velocity components in the vehicle coordinate system, and v_{veh} represents the vehicle motion velocity, which is obtained from the BeiDou GNSS; $\boldsymbol{\omega}$ is the angular velocity vector induced by the variation of vehicle attitude, and ω_x, ω_y and ω_z denote the angular velocities about the vehicle x-, y-, and z-axes, respectively. The symbols ϕ, θ, and ψ represent the roll, pitch, and heading (yaw) angles, respectively, and the overdot denotes the time derivative. The sign conventions for the attitude angles are defined as follows. When viewed along the positive x-axis, a clockwise rotation about the x-axis, or a tilt to the left of the driver view, is defined as a positive roll angle ϕ. When viewed along the positive y-axis, a clockwise rotation about the y-axis is defined as a positive pitch angle θ, such that $\theta > 0$ corresponds to a downward tilt of the vehicle front. The heading (yaw) angle ψ is defined as 0° pointing to geographic north and increases clockwise (Campbell Scientific, 2019). The roll and pitch angles, ϕ and θ, are directly provided by the CSAT3B, while the heading angle ψ is obtained from the high-precision digital compass installed on the vehicle. To reduce the amplification of high-frequency noise during numerical differentiation, the attitude angles were smoothed prior to calculating the angular velocity. The vector $\boldsymbol{r}$ represents the position vector from the vehicle center of mass to the center of the anemometer sensor. Since the exact position of the vehicle center of mass is difficult to determine, the geometric center of the vehicle body is used as an approximation in this study. According to the installation position of the sensor, the components of $\boldsymbol{r}$ are determined as $r_x = -1.880$ m, $r_y = 0$, and $r_z = 1.386$ m. Since $r_y = 0$, Eq. (30) can be further simplified as follows:

$$\boldsymbol{\omega} \times \boldsymbol{r} = \begin{bmatrix} -\dot{\theta} r_z \\ -\dot{\psi} r_x - \dot{\phi} r_z \\ \dot{\theta} r_x \end{bmatrix}. \tag{31}$$

It should be noted that the wind velocity components obtained from Eq. (31) are still defined in the vehicle coordinate system. The heading angle provided by the digital compass is additionally required to transform the wind velocity into the standard geographic coordinate system. This coordinate transformation procedure is consistent with the processing framework proposed by Belusic et al. (2014).

Specifically, the three-dimensional wind velocity components (v_{ex},v_{ey}, v_{ez}) defined in the vehicle coordinate system are transformed into the north–east–up (NEU) coordinate system using a direction cosine matrix (DCM). The corresponding wind velocity components (v_N, u_E, w_U) can be expressed as

$$\begin{bmatrix} v_N \\ u_E \\ w_U \end{bmatrix} = \mathrm{DCM}(\phi, \theta, \psi) \left(\begin{bmatrix} v_{ex} \\ v_{ey} \\ v_{ez} \end{bmatrix} \right), \tag{32}$$

where the direction cosine matrix $\mathrm{DCM}(\phi, \theta, \psi)$ is defined as

$$\mathrm{DCM}(\phi, \theta, \psi) = \begin{bmatrix} \cos\psi & -\sin\psi & 0 \\ \sin\psi & \cos\psi & 0 \\ 0 & 0 & 1 \end{bmatrix} \begin{bmatrix} \cos\theta & 0 & -\sin\theta \\ 0 & 1 & 0 \\ \sin\theta & 0 & \cos\theta \end{bmatrix} \begin{bmatrix} 1 & 0 & 0 \\ 0 & \cos\phi & -\sin\phi \\ 0 & \sin\phi & \cos\phi \end{bmatrix}, \tag{33}$$

https://doi.org/10.5194/egusphere-2026-2441
Preprint. Discussion started: 2 July 2026

and v_N, u_E, and w_U denote the corrected three-dimensional wind velocity components in the northward, eastward, and vertical directions, respectively. The construction of the DCM using Eq. (33) explicitly accounts for the sign conventions adopted by the CSAT3B for the pitch and heading angles. Corresponding modifications are incorporated into the matrix formulation, such that the overall transformation is equivalent to a standard right-handed rotation, thereby ensuring consistency in physical interpretation.

3.3.3 Overall framework for vehicle-mounted three-dimensional wind velocity correction

By combining the vehicle-induced flow distortion correction algorithm established in Section 3.3.1 with the vehicle motion compensation, attitude compensation, and coordinate transformation procedures described in Section 3.3.2, a complete vehicle-mounted three-dimensional wind velocity correction algorithm can be constructed. Accordingly, under any inflow directions, a singular correction formulation for the vehicle-mounted three-dimensional wind velocity can be written as

$$\begin{bmatrix} v_N \\ u_E \\ w_U \end{bmatrix} = \mathrm{DCM}(\phi,\theta,\psi)(\boldsymbol{v}_m - \Delta\boldsymbol{V}_A - \Delta\boldsymbol{V}_D - \Delta\boldsymbol{V}_V), \tag{34}$$

$$\boldsymbol{v}_m = \begin{bmatrix} v_{mx} \\ v_{my} \\ v_{mz} \end{bmatrix}, \tag{35}$$

$$\Delta\boldsymbol{V}_A = \begin{bmatrix} \dot{\theta} r_z \\ \dot{\psi} r_x + \dot{\phi} r_z \\ -\dot{\theta} r_x \end{bmatrix}, \tag{36}$$

$$\Delta\boldsymbol{V}_D = \begin{bmatrix} \Delta v_x^{H/TW} \\ \Delta v_y^{H/TW} \\ \Delta v_z^{H/TW} \end{bmatrix}, \tag{37}$$

$$\Delta\boldsymbol{V}_V = \begin{bmatrix} v_{veh} \\ 0 \\ 0 \end{bmatrix}, \tag{38}$$

where $\boldsymbol{v}_m$ denotes the three-dimensional wind velocity measured by the vehicle-mounted anemometer in the sensor coordinate system. The terms $\Delta\boldsymbol{V}_A$, $\Delta\boldsymbol{V}_D$, and $\Delta\boldsymbol{V}_V$ represent the additional velocity components induced by vehicle attitude motion, flow distortion around the vehicle body, and vehicle translation, respectively.

3.4 Evaluation of correction performance

In the experiment described in Section 2.3, vehicle-mounted and ground-based wind measurements were acquired simultaneously. The ground-based wind data were processed using the same attitude compensation and coordinate transformation procedures as those applied to the vehicle-mounted measurements, yielding the corrected three-dimensional ground wind velocity in the geographic coordinate system (the NEU system), denoted as $\boldsymbol{V}_G$. The vehicle-mounted wind data were processed following two different workflows. In the first workflow, the complete correction procedure described in Eq.

https://doi.org/10.5194/egusphere-2026-2441
Preprint. Discussion started: 2 July 2026

(34) was applied, resulting in the final corrected three-dimensional vehicle-mounted wind velocity, denoted as $\boldsymbol{V}_{\mathrm{C}}$. In the second workflow, only the vehicle motion compensation, attitude compensation, and coordinate transformation were applied, yielding the three-dimensional vehicle-mounted wind velocity but still affected by vehicle-induced flow distortion, denoted as $\boldsymbol{V}_{\mathrm{O}}$. The present study primarily focuses on a comparative analysis of the three wind velocity datasets $\boldsymbol{V}_{\mathrm{O}}$, $\boldsymbol{V}_{\mathrm{C}}$, and $\boldsymbol{V}_{\mathrm{G}}$. In the following analyses, wind speed refers to the horizontal wind speed, while the vertical wind component w is analyzed separately. Considering that headwind and tailwind conditions differ in both occurrence frequency and correction strategies, the comparison results are presented separately in Sections 3.4.1 and 3.4.2.

3.4.1 Correction performance under headwind conditions

During the experiment, more than 95% of the valid observations corresponded to headwind driving conditions. Even when the ambient wind approached the vehicle from behind, the wind still exhibited headwind characteristics in the vehicle coordinate system after vehicle motion compensation was applied. Under typical urban driving conditions, the vehicle speed generally ranges from 15 to 30 km h^{-1}, but can be considerably higher depending on traffic or the need for driving speeds. Within this speed range, the vehicle-mounted wind measurements are almost exclusively associated with headwind conditions or oblique inflow conditions which can be broken down into headwind and cross wind components. Therefore, wind velocity correction under headwind/oblique wind conditions constitutes the primary focus of this study.

Under headwind conditions, approximately 15 h of valid observations were obtained, corresponding to about 54,000 instantaneous wind data points. To enable a comparison between instantaneous vehicle-mounted and ground-based wind velocities, a data selection strategy is needed. Specifically, only the vehicle-mounted wind measurements acquired while the vehicle was traveling on the same side of the road as the ground-based anemometer and within a distance range of 5–15 m before arriving at the ground anemometer position were selected for comparison, typically comprising 1–6 data points for each passing of vehicle by the ground site. The primary rationale for adopting this strategy is that such observations are less affected by local disturbances induced by the ground-based anemometer itself and surrounding structures, and that any vehicle induced wake flow disturbances have not yet affected the ground-based anemometer measurements. Moreover, under these conditions, the vehicle-mounted and ground-based anemometers can be considered to sample the same incoming flow in space and time, thereby enabling a consistency of the instantaneous wind velocity comparison.

In addition, to further ensure the reliability of the comparison results, data points exhibiting wind speed magnitudes or wind direction differences that deviated substantially from the overall distribution of the data during each vehicle pass were manually excluded. The remaining instantaneous observations were then used for the comparative analysis between vehicle-mounted and ground-based wind velocities. It should be noted that the field validation data in this study primarily cover a true wind speed range of 0–4 m s^{-1} based on the ground-based measurements, which represents wind conditions with relatively high frequencies in near-surface mobile observations. Under higher wind speed conditions, the available data are comparatively limited, and therefore a systematic statistical analysis for the higher winds was not conducted in this study. These higher wind speed conditions will be further investigated and supplemented in future work.

https://doi.org/10.5194/egusphere-2026-2441
Preprint. Discussion started: 2 July 2026

Figure 9 presents a comparison between the vehicle-mounted wind velocities before and after correction and the ground-based anemometer observations under headwind conditions. As shown in Fig. 9(a), the relative deviation of $\boldsymbol{V}_{\mathrm{O}}$ with respect to $\mathbf{V}_{\mathrm{G}}$ exhibits pronounced scatter at low wind speeds, with deviations exceeding ±300% for some samples. This indicates that vehicle-induced flow distortion has a substantial impact on vehicle-mounted wind velocity measurements under headwind conditions. In contrast, the relative deviations of $\boldsymbol{V}_{\mathrm{C}}$ are markedly reduced across all wind speed ranges, with a significantly smaller number of extreme outliers. The deviation distribution of $\boldsymbol{V}_{\mathrm{C}}$ is more concentrated around zero, and its overall deviation magnitude is substantially smaller than that of $\boldsymbol{V}_{\mathrm{O}}$. Figure 9(b) shows the distributions of absolute errors of $\boldsymbol{V}_{\mathrm{O}}$ and $\boldsymbol{V}_{\mathrm{C}}$ relative to $\boldsymbol{V}_{\mathrm{G}}$, after binning by the wind speed magnitude of $\boldsymbol{V}_{\mathrm{G}}$. Overall, the absolute errors of $\boldsymbol{V}_{\mathrm{C}}$ are consistently smaller than those of $\boldsymbol{V}_{\mathrm{O}}$ across all wind speed intervals, and the error distributions are noticeably narrower. As wind speed increases, the dispersion of errors associated with $\boldsymbol{V}_{\mathrm{O}}$ becomes progressively larger, with some samples exhibiting pronounced deviations, whereas the error distribution of $\boldsymbol{V}_{\mathrm{C}}$ remains comparatively concentrated in narrower ranges. Consistent with the quantitative statistics summarized in Table 2, within the wind speed intervals of 0–1 m s^{-1}, 1–2 m s^{-1}, 2–3 m s^{-1}, and 3–4 m s^{-1}, the mean bias error (MBE) of $\boldsymbol{V}_{\mathrm{C}}$ is reduced by 25.0%, 81.2%, 82.9%, and 91.1%, respectively, compared with $\boldsymbol{V}_{\mathrm{O}}$. The corresponding reductions in root-mean-square error (RMSE) are 14.5%, 16.9%, 12.6%, and 15%. These results demonstrate that, under headwind conditions, the proposed flow disturbance correction algorithm can effectively reduce both systematic biases and random errors in vehicle-mounted wind velocity measurements, while exhibiting consistent correction performance across different wind speed ranges.

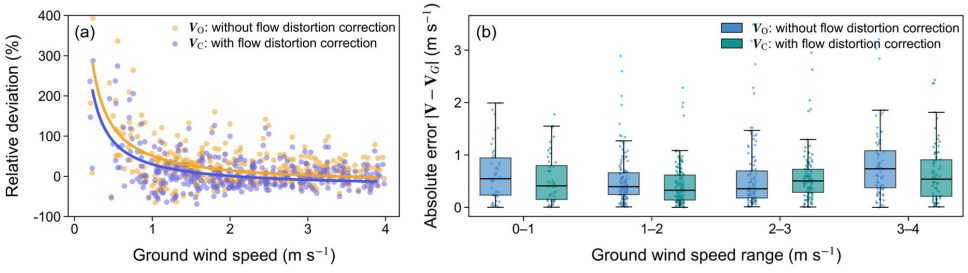

Figure 9: Comparison of vehicle-mounted wind velocities before and after correction with ground-based wind measurements under headwind conditions. (a) Relative deviations of the disturbed wind velocity $\boldsymbol{V}_{\mathrm{O}}$ and the corrected wind velocity $\boldsymbol{V}_{\mathrm{C}}$ with respect to the ground-based wind velocity $\boldsymbol{V}_{\mathrm{G}}$. The solid lines represent fitted curves using a rational function of the form y = a/(x + b) + c; (b) Distributions of absolute errors of $\boldsymbol{V}_{\mathrm{O}}$ and $\boldsymbol{V}_{\mathrm{C}}$ relative to $\boldsymbol{V}_{\mathrm{G}}$, after binning by the wind speed magnitude of $\boldsymbol{V}_{\mathrm{G}}$.

On this basis, Fig. 10 further compares the wind rose distributions of vehicle-mounted wind directions before and after correction with those measured by the ground-based anemometer under headwind conditions. Consistent with the quantitative statistics of the mean absolute wind direction error summarized in Table 2, within the wind speed intervals of 0–1 m s^{-1}, 1–2

https://doi.org/10.5194/egusphere-2026-2441
Preprint. Discussion started: 2 July 2026

m s^{-1}, 2–3 m s^{-1}, and 3–4 m s^{-1}, the mean absolute error (MAE) of the corrected wind direction is reduced by 17.4%, 10.0%, 6.6%, and 8.7%, respectively. In these true wind speed ranges, the ratio $\boldsymbol{V}_C/\boldsymbol{V}_G$ is 1.67, 1.04, 1.02, and 1.01, respectively, clearly showing excellent retrieval of the true instantaneous wind speed using the vehicle-mounted anemometer and subsequent correction algorithm. In addition, as wind speed increases, the wind directions of both $\boldsymbol{V}_O$ and $\boldsymbol{V}_C$ tend to become closer to that of $\boldsymbol{V}_G$. These results indicate that the proposed correction method is also effective in improving the accuracy of vehicle-mounted wind direction measurements under headwind conditions.

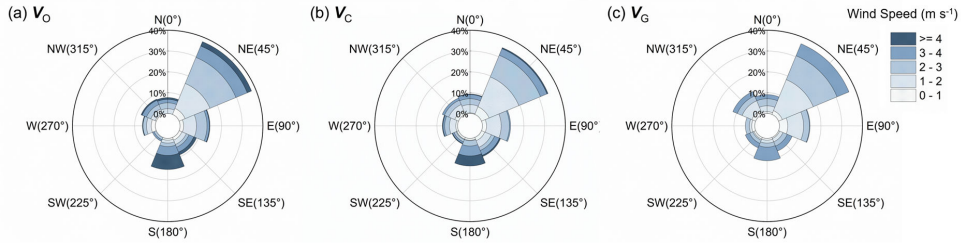

Figure 10: Comparison of wind rose distributions of vehicle-mounted wind directions before and after correction with ground-based wind direction measurements under headwind conditions. (a) $\boldsymbol{V}_O$; (b) $\boldsymbol{V}_C$; (c) $\boldsymbol{V}_G$.

In addition, the statistical results of the vertical wind velocity component $w$further validate. the overall correction capability of the proposed method. Compared with the uncorrected results, the mean bias error (MBE) of w is reduced by 30.6%, 51.5%, 54.2%, and 87.2% within the aforementioned wind speed intervals, respectively. The corresponding reductions in root-mean-square error (RMSE) are 31.9%, 39.0%, 36.7%, and 53.3%.

Taken together with the comparison results for wind speed, wind direction, and the vertical wind velocity component, it can be concluded that the proposed flow disturbance correction algorithm can significantly improve the consistency between vehicle-mounted three-dimensional wind velocity measurements and ground-based reference observations under headwind conditions. Such an agreement provides reliable technical supports for mobile atmospheric observations under complex driving conditions.

Table 2. Quantitative statistical results of the vehicle-mounted wind velocity correction performance under headwind conditions.

Evaluation metric		Wind speed range (m s^{-1})			
		0–1	1–2	2–3	3–4
Number of nearest-neighbor matched samples		44	129	103	78
MBE of wind speed (m s^{-1})	$\boldsymbol{V}_O$	0.60	0.32	0.35	0.45
	$\boldsymbol{V}_C$	0.45	0.06	0.06	0.04

https://doi.org/10.5194/egusphere-2026-2441
Preprint. Discussion started: 2 July 2026

RMSE of wind speed (m s^{-1})	$\boldsymbol{V}_O$	0.83	0.71	0.87	1.00
	$\boldsymbol{V}_C$	0.71	0.59	0.76	0.85
MAE of wind direction (°)	$\boldsymbol{V}_O$	44.8	19.7	12.1	11.5
	$\boldsymbol{V}_C$	37.0	17.8	11.3	10.5
MBE of vertical wind velocity w (m s^{-1})	$\boldsymbol{V}_O$	0.62	0.68	0.59	0.94
	$\boldsymbol{V}_C$	-0.43	-0.33	-0.27	-0.12
RMSE of vertical wind velocity w (m s^{-1})	$\boldsymbol{V}_O$	0.91	0.95	0.90	1.22
	$\boldsymbol{V}_C$	0.62	0.58	0.57	0.57

Note: MBE denotes the mean bias error, and RMSE denotes the root-mean-square error. Wind direction errors are calculated using a circular difference, defined as $\min(|\alpha - \alpha_G|, 360° - |\alpha - \alpha_G|)$, where α and α_G represent the wind directions measured by the vehicle-mounted and ground-based anemometers, respectively.

3.4.2 Correction performance under tailwind conditions

In practical mobile observations, tailwind conditions occur less frequently. However, they may still arise when the vehicle speed is relatively low and the ambient wind speed is comparatively high. Compared with headwind conditions, the flow field structure under tailwind conditions is more complex, and the vehicle wake exerts a pronounced influence on the vehicle-mounted wind velocity measurements. In view of these characteristics, the three-dimensional wind velocity correction method for tailwind conditions in Section 3.3.1 needs evaluation separately.

Under tailwind conditions, approximately 3000 instantaneous observation data samples were obtained in this study. Most of the samples were collected when the vehicle speed was relatively low (≤20 km h^{-1}). The overall data volume is limited, which makes it difficult to apply the same stringent data screening and analysis criteria as those used for headwind conditions. Accordingly, for the evaluation under tailwind conditions, the vehicle-mounted wind velocity measurements are directly compared with the ground-based anemometer observations acquired at the same time. Similar to the headwind analysis, data points with wind speed magnitudes or wind direction differences that deviate substantially from the overall distribution are manually excluded. In addition, considering that the ground-based anemometer is also affected by the wake of its battery compartment under direct tailwind conditions, the corresponding contaminated data are excluded from the comparison. As a result, the validation data obtained under tailwind conditions primarily cover a wind speed range of 1–5 m s^{-1}.

Similarly, Fig. 11 presents a comparison between vehicle-mounted wind velocities before and after correction and the ground-based anemometer observations under tailwind conditions. It can be seen that, across all wind speed ranges, the relative deviations and absolute errors of $\boldsymbol{V}_C$ exhibit an overall convergence tendency with increased wind speeds. The number of extreme outliers is markedly reduced, and the overall error magnitude is smaller than that of $\boldsymbol{V}_O$. According to the quantitative statistics summarized in Table 3, within the wind speed intervals of 1–2 m s^{-1}, 2–3 m s^{-1}, and 3–4 m s^{-1}, the wind speed MBE of $\boldsymbol{V}_C$ is reduced by 12.2%, 31.0%, and 82.1%, respectively, compared with $\boldsymbol{V}_O$. The corresponding reductions in RMSE are 11.0%, 15.4%, and 14.5%. Within the wind speed range of 4–5 m s^{-1}, the MBE values of both datasets are relatively small,

https://doi.org/10.5194/egusphere-2026-2441
Preprint. Discussion started: 2 July 2026

with absolute values below 0.20 m s^{-1}. However, the RMSE of $\boldsymbol{V}_C$ is still reduced by 13.1% compared with that of $\boldsymbol{V}_O$. With increasing wind speed, the MBE values of both $\boldsymbol{V}_O$ and $\boldsymbol{V}_C$ show an overall decreasing trend. In contrast, the absolute variation in RMSE remains relatively limited. This suggests that, under tailwind conditions, the correction method is primarily effective in reducing systematic bias, whereas the improvement in random error is comparatively limited.

Overall, under tailwind conditions, the proposed flow distortion correction algorithm is capable of reducing both systematic bias and random error in vehicle-mounted wind velocity measurements. However, the improvement is weaker than that achieved under headwind conditions. This difference mainly arises from the more complex wake-induced flow distortion under tailwind conditions. In addition, the samples available for comparison exhibit weaker spatial and temporal consistency, which further limits the potential for improvement in correction performance.

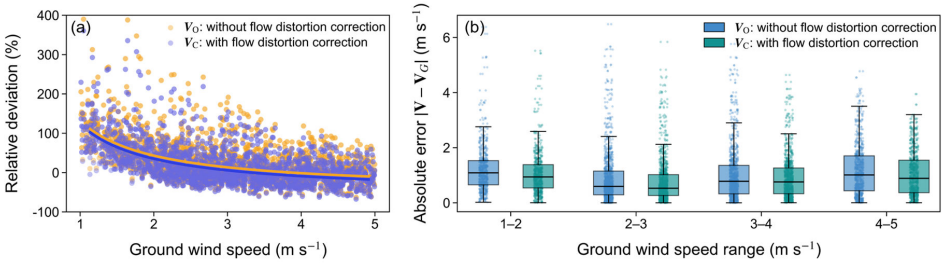

Figure 11: Comparison of vehicle-mounted wind velocities before and after correction with ground-based wind measurements under tailwind conditions. (a) Relative deviations of the disturbed wind velocity $\boldsymbol{V}_O$ and the corrected wind velocity $\boldsymbol{V}_C$ with respect to the ground-based wind velocity $\boldsymbol{V}_G$. The solid lines represent fitted curves using a rational function of the form y = a/(x + b) + c; (b) Distributions of absolute errors of $\boldsymbol{V}_O$ and $\boldsymbol{V}_C$ relative to $\boldsymbol{V}_G$, after binning by the wind speed magnitude of $\boldsymbol{V}_G$.

Under tailwind conditions, the wind directions before and after correction are further compared with the ground-based wind direction observations, as shown in Fig. 12. Combined with the quantitative statistics of the mean absolute wind direction error presented in Table 3, it can be observed that, compared with headwind conditions, the overall improvement in circular wind direction error under tailwind conditions is relatively limited. At the same time, the MBE and RMSE of the vertical wind velocity component w are already at relatively low levels compared with those under headwind conditions, and the differences before and after correction are not pronounced. These results indicate that, under tailwind conditions, the performance of the correction method for wind direction and the vertical wind velocity component is relatively limited, despite the aforementioned improvements in the correction for wind speeds measured by the vehicle-mounted platform under tailwind conditions. This limitation is mainly attributable to the reduced consistency of the data samples available for the comparative analysis. This result further suggests that, for improving the correction performance of wind direction and the vertical wind velocity component under tailwind conditions, it is necessary to acquire more data to improve result robustness.

https://doi.org/10.5194/egusphere-2026-2441
Preprint. Discussion started: 2 July 2026

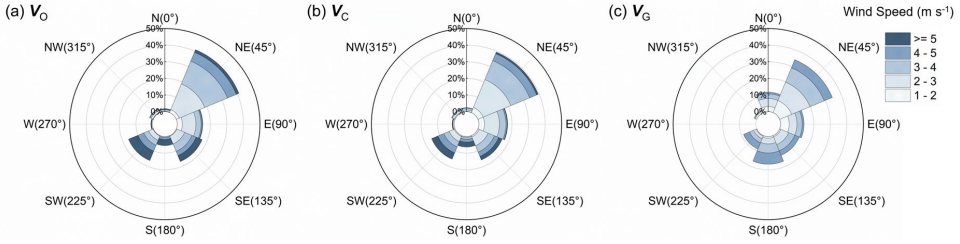

Figure 12: Comparison of wind rose distributions of vehicle-mounted wind directions before and after correction with ground-based wind direction measurements under tailwind conditions. (a) V_O; (b) V_C; (c) V_G.

725

Table 3. Quantitative statistical results of the vehicle-mounted wind velocity correction performance under tailwind conditions.

Evaluation metric		Wind speed range (m s^{-1})			
		1–2	2–3	3–4	4–5
Total number of samples in straight driving segments		675	1132	984	742
MBE of wind speed (m s^{-1})	V_O	1.23	0.71	0.39	0.20
	V_C	1.08	0.49	0.07	-0.20
RMSE of wind speed (m s^{-1})	V_O	1.54	1.36	1.45	1.53
	V_C	1.37	1.15	1.24	1.33
MAE of wind direction (°)	V_O	28.6	22.2	19.5	19.1
	V_C	28.6	22.3	19.5	19.4
MBE of vertical wind velocity w (m s^{-1})	V_O	-0.07	0.04	0.15	0.21
	V_C	-0.22	-0.16	-0.10	-0.08
RMSE of vertical wind velocity w (m s^{-1})	V_O	0.52	0.56	0.64	0.75
	V_C	0.57	0.59	0.66	0.75

3.5 Relative contributions of attitude variations and flow distortion to measurement errors

The effectiveness of the complete correction method has been demonstrated in Sect. 3.4. However, the specific sources of measurement errors are still not fully accounted for. One of the sources is the false sensor signals from vehicle attitude changes
730 during driving, as given in the explicit correction framework that accounts for the additional velocity induced by attitude variations (i.e., “apparent wind”), an effect that is typically neglected in previous studies (Belusic et al., 2014; Hanlon and Risk, 2020; Miller et al., 2019; Miller and Gordon, 2022). To further quantify the contributions of attitude changes to measurement biases, this section quantifies the false wind signals introduced by attitude variations and compare them to those due to flow distortions. The validation experiment in Sect. 3.4 was mainly conducted on straight and flat road segments. As a

https://doi.org/10.5194/egusphere-2026-2441
Preprint. Discussion started: 2 July 2026

result, the magnitude of attitude variations was limited, and their impact could not be fully assessed. To better compare the contributions of attitude variations and flow distortion under more realistic driving conditions, a continuous 4 h dataset collected on 17 May is used. This dataset includes a range of driving states, such as lane changes, bumps, and U-turns. Within the unified correction framework, the contributions of the attitude-related term and the flow-distortion term are calculated after coordinate transformation. These contributions are then normalized by the corrected horizontal wind speed $\boldsymbol{V}_{\mathrm{C}}$, allowing a direct comparison of their relative magnitudes.

First, under the unified coordinate transformation framework given by Eq. (34), the additional velocities induced by attitude variations and flow distortion are defined as the contribution vectors of the attitude-related term and the flow-distortion term, denoted as $\mathbf{C}_{\mathrm{A}}$ and $\mathbf{C}_{\mathrm{D}}$, respectively. Based on the direction cosine matrix (DCM), these vectors can be transformed from the vehicle coordinate system to the Earth-referenced coordinate system, expressed as:

$$\boldsymbol{C}_{\mathrm{A}} = \mathrm{DCM}(\phi, \theta, \psi)\Delta\boldsymbol{V}_{\mathrm{A}}. \tag{39}$$

$$\boldsymbol{C}_{\mathrm{D}} = \mathrm{DCM}(\phi, \theta, \psi)\Delta\boldsymbol{V}_{\mathrm{D}}. \tag{40}$$

Based on the contribution vectors defined above, two contribution ratios, R_{A} and R_{D}, are introduced to quantify the relative contributions of attitude variations and flow distortion to the measurement error. Since this study focuses on the horizontal wind speed, the following analysis is restricted to the horizontal components. Specifically, the magnitudes of the horizontal components of the contribution vectors are denoted as $|\,\mathbf{C}_{\mathrm{A}}^{\mathrm{h}}\,|$and $|\,\mathbf{C}_{\mathrm{D}}^{\mathrm{h}}\,|$. These quantities are normalized by the corrected horizontal wind speed $\boldsymbol{V}_{\mathrm{C}}$, yielding

$$R_{\mathrm{A}} = \frac{\left|\boldsymbol{C}_{\mathrm{A}}^{\mathrm{h}}\right|}{\boldsymbol{V}_{\mathrm{C}}}, \tag{41}$$

$$R_{\mathrm{D}} = \frac{\left|\boldsymbol{C}_{\mathrm{D}}^{\mathrm{h}}\right|}{\boldsymbol{V}_{\mathrm{C}}}, \tag{42}$$

where $\left|\boldsymbol{C}^{\mathrm{h}}\right| = \sqrt{C_x^2 + C_y^2}$ represents the magnitude of the contribution vector in the horizontal plane, and $\boldsymbol{V}_{\mathrm{C}}$ is the corrected horizontal wind speed. R_{A} and R_{D} denote the relative contributions of attitude variations and flow distortion to the measurement error in horizontal wind speed, respectively.

Figure 13 shows the relative contributions of attitude variations and flow distortions to the measurement errors of horizontal wind speed under different wind speed conditions. Panel (a) presents the overall distribution for all samples, while panel (b) further groups the data according to the corrected wind speed. From the overall distribution, the contribution from flow distortion, R_{D}, is clearly larger than that from attitude variations, R_{A}. As shown in Fig. 13(a), the median of R_{D} is around 15%, whereas R_{A} is mainly concentrated below 5%. This indicates that, in a statistical sense, vehicle-induced flow distortion is the dominant source of measurement error in the vehicle-mounted wind observations. However, it should be noted that although the typical magnitude of R_{A} is relatively small, its distribution still shows noticeable variability. In some cases, R_{A} can reach relatively high values, suggesting that attitude variations can have significant impacts on instantaneous measurements under certain conditions and therefore cannot be neglected. Furthermore, Fig. 13(b) shows that the contributions from both error

https://doi.org/10.5194/egusphere-2026-2441
Preprint. Discussion started: 2 July 2026

sources decrease with increasing wind speed, and their distributions become more confined to narrow bands. In the low wind speed range (0.5–1 m s^{-1}), the median value of R_D exceeds 30%, with a relatively wide spread. This indicates that under weak inflow conditions, vehicle-induced flow distortion dominates the measurement error. As wind speed increases, R_D gradually decreases, reaching about 15% when wind speed exceeds 4 m s^{-1}. This trend suggests that the relative impact of flow distortion becomes weaker under stronger ambient wind conditions. In comparison, the contribution from attitude variations, R_A, remains consistently lower than R_D across all wind speed ranges. Its typical values are generally below 10% and show a slight decreasing trend with increasing wind speed. This is mainly because the additional velocity induced by attitude variations is limited in magnitude. However, under low wind speed conditions or during more dynamic vehicle motions (e.g., turning or bumping), R_A can still increase noticeably. This suggests that the impact of attitude variations is closely related to the specific states of vehicle motion and can be non-negligible when the vehicle attitude experiences large changes.

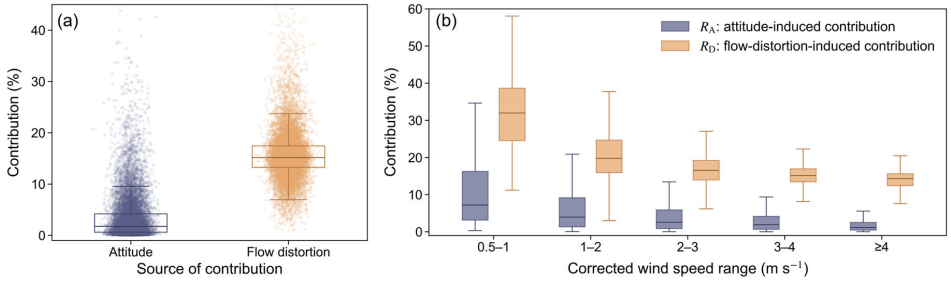

Figure 13: Relative contributions of attitude variations and flow distortion to the measurement error of horizontal wind speed. (a) Overall distribution for all samples; (b) distributions grouped by corrected wind speed ranges.

4 Summary and conclusions

Vehicle-mounted wind measurement platforms provide an important means for observing near-surface wind fields with high spatial and temporal resolutions. However, vehicle-induced flow distortions, vehicle motion, and attitude variations can all exert significant influences on vehicle-mounted wind measurements, leading to systematic deviations of the measured wind vectors from the true ambient wind field. To address this issue, this study pursues a CFD-based parameterization approach for correcting vehicle-mounted three-dimensional instantaneous wind velocity measurements. The method is designed to systematically correct the effects of vehicle-induced flow distortions on wind measurements. By conducting parameterized CFD simulations under multiple inflow wind speed and wind direction conditions within a unified computational algorithm, a functional relationship linking the true incoming wind velocity and the disturbed wind velocity measured by the anemometer is established. This approach avoids the need to repeatedly reconstruct the computational domain and perform CFD simulations for different inflow conditions, thereby enabling efficient and unified correction of vehicle-mounted three-dimensional wind

https://doi.org/10.5194/egusphere-2026-2441
Preprint. Discussion started: 2 July 2026

velocity. In addition, the proposed method simultaneously accounts for vehicle motion compensation, attitude compensation, and coordinate transformation. It is therefore applicable to the processing of vehicle-mounted wind measurements under a wide range of driving conditions.

The ground-based validation experiments demonstrate that, under headwind conditions, the proposed correction method can substantially reduce both systematic biases and random errors in vehicle-mounted measurements of wind speed, wind direction, and the vertical wind velocity component. Consequently, the agreement between vehicle-mounted observations and ground-based reference measurements is significantly improved. Under tailwind conditions, the correction performance is relatively weaker than that under headwind conditions, mainly due to the strong influence of the vehicle wake and the limited availability of validation data. Nevertheless, the corrected wind speed magnitude still shows an overall improvement compared with the uncorrected measurements, indicating that the proposed method maintains a reasonable level of robustness under more complex flow conditions. In addition, the contribution analysis shows that flow distortion is the dominant source of measurement error in vehicle-mounted wind observations, while the contribution from attitude variations is smaller. As the ambient wind speed increases, the relative contributions of both error sources decrease. However, under low wind speed conditions or during more dynamic vehicle motions (e.g., turning or bumping), the impact of attitude variations can increase noticeably. Therefore, in the correction process, priority should be given to compensating for flow distortion, while the additional effects induced by attitude variations should also be taken into account to improve the stability and reliability of the measurements. More importantly, to the best of our knowledge, this study represents the first attempt to establish a systematic correction algorithm for mobile three-dimensional wind measurements based on CFD-derived parameterization, while simultaneously accounting for the effects of vehicle attitude variations. By constructing a functional relationship between the true incoming wind velocity and the distorted wind velocity measured by the vehicle-mounted anemometer, the correction algorithm enables efficient reconstruction of the ambient wind field without the need for repeated CFD simulations under different inflow conditions. The proposed approach therefore provides a practical pathway for obtaining reliable three-dimensional wind measurements from vehicle-mounted platforms. Such a pathway contributes to the advancement of mobile atmospheric wind observation techniques and offers a promising methodology for high-resolution measurements of near-surface wind fields and atmospheric boundary-layer processes.

Data availability

Data are available from the corresponding author upon reasonable request.

Author contributions

KC conducted the CFD simulations, performed the data analysis, and drafted the initial manuscript. YY contributed to the confirmation of CFD simulation parameters and the development of the correction algorithm. YH, YZ, and JZ participated in

https://doi.org/10.5194/egusphere-2026-2441
Preprint. Discussion started: 2 July 2026

the validation experiments. HS and CL assisted in refining the correction algorithm. LK provided the software platform and supported the computational implementation of the CFD simulations. KL and ZW assisted in improving the data analysis methods. SML provided guidance on the correction algorithm and reviewed and edited the manuscript to ensure the accuracy and completeness of the study.

Competing interests

At least one of the (co-)authors is a member of the editorial board of Atmospheric Measurement Techniques.

Disclaimer

Copernicus Publications remains neutral with regard to jurisdictional claims made in the text, published maps, institutional affiliations, or any other geographical representation in this paper. While Copernicus Publications makes every effort to include appropriate place names, the final responsibility lies with the authors. Views expressed in the text are those of the authors and do not necessarily reflect the views of the publisher.

Financial support

This project was supported by a grant from the National Natural Science Foundation of China Creative Research Group Fund (Grant No. 22221004).

References

Apte, J. S., Messier, K. P., Gani, S., Brauer, M., Kirchstetter, T. W., Lunden, M. M., Marshall, J. D., Portier, C. J., Vermeulen, R. C. H., and Hamburg, S. P.: High-resolution air pollution mapping with Google street view cars: exploiting big data, Environ. Sci. Technol., 51, 6999–7008, https://doi.org/10.1021/acs.est.7b00891, 2017.

Belusic, D., Lenschow, D. H., and Tapper, N. J.: Performance of a mobile car platform for mean wind and turbulence measurements, Atmos. Meas. Tech., 7, 1825–1837, https://doi.org/10.5194/amt-7-1825-2014, 2014.

Brantley, H. L., Thoma, E. D., Squier, W. C., Guven, B. B., and Lyon, D.: Assessment of methane emissions from oil and gas production pads using mobile measurements, Environ. Sci. Technol., 48, 14508–14515, https://doi.org/10.1021/es503070q, 2014.

Broniszewski, J. and Piechna, J.: A fully coupled analysis of unsteady aerodynamics impact on vehicle dynamics during braking, Eng. Appl. Comput. Fluid Mech., 13, 623–641, https://doi.org/10.1080/19942060.2019.1616326, 2019.

Campbell Scientific, Inc.: CSAT3B three-dimensional sonic anemometer instruction manual, Campbell Scientific, Inc., Logan, Utah, USA, 2019.

https://doi.org/10.5194/egusphere-2026-2441
Preprint. Discussion started: 2 July 2026

Edie, R., Robertson, A. M., Field, R. A., Soltis, J., Snare, D. A., Zimmerle, D., Bell, C. S., Vaughn, T. L., and Murphy, S. M.: Constraining the accuracy of flux estimates using OTM 33A, Atmos. Meas. Tech., 13, 341–353, https://doi.org/10.5194/amt-13-341-2020, 2020.

Erland, B. M., Thorpe, A. K., and Gamon, J. A.: Recent advances toward transparent methane emissions monitoring: a review, Environ. Sci. Technol., 56, 16567–16581, https://doi.org/10.1021/acs.est.2c02136, 2022.

Foken, T.: 50 years of the monin–obukhov similarity theory, Boundary Layer Meteorol., 119, 431–447, https://doi.org/10.1007/s10546-006-9048-6, 2006.

Gordon, M., Staebler, R. M., Liggio, J., Makar, P., Li, S.-M., Wentzell, J., Lu, G., Lee, P., and Brook, J. R.: Measurements of enhanced turbulent mixing near highways, J. Appl. Meteorol. Climatol., 51, 1618–1632, https://doi.org/10.1175/JAMC-D-11-0190.1, 2012.

Griessbaum, F., Moat, B. I., Narita, Y., Yelland, M. J., Klemm, O., and Uematsu, M.: Uncertainties in wind speed dependent CO2 transfer velocities due to airflow distortion at anemometer sites on ships, Atmos. Chem. Phys., 10, 5123–5133, https://doi.org/10.5194/acp-10-5123-2010, 2010.

Grimmond, C. S. B. and Oke, T. R.: Aerodynamic properties of urban areas derived from analysis of surface form, 1999.

Hanlon, T. and Risk, D.: Using computational fluid dynamics and field experiments to improve vehicle-based wind measurements for environmental monitoring, Atmos. Meas. Tech., 13, 191–203, https://doi.org/10.5194/amt-13-191-2020, 2020.

Houston, A. L., Laurence, R. J., Nichols, T. W., Waugh, S., Argrow, B., and Ziegler, C. L.: Intercomparison of unmanned aircraftborne and mobile mesonet atmospheric sensors, J. Atmos. Oceanic Technol., 33, 1569–1582, https://doi.org/10.1175/JTECH-D-15-0178.1, 2016.

Hu, T., Qi, S., Qiu, Z., Zou, J., and Wang, D.: Application of PSO-LSSVM in Bias Correction of Shipborne Anemometer Measurement, in: Cognitive Systems and Signal Processing, vol. 1005, edited by: Sun, F., Liu, H., and Hu, D., Springer Singapore, Singapore, 348–357, https://doi.org/10.1007/978-981-13-7983-3_31, 2019.

Kurec, K.: Numerical study of the sports car aerodynamic enhancements, Energies, 15, 6668, https://doi.org/10.3390/en15186668, 2022.

Leśniewicz, P., Kulak, M., and Karczewski, M.: Aerodynamic analysis of an isolated vehicle wheel, J. Phys. Conf. Ser., 530, 12064, https://doi.org/10.1088/1742-6596/530/1/012064, 2014.

Li, Z., Guo, J., Ding, A., Liao, H., Liu, J., Sun, Y., Wang, T., Xue, H., Zhang, H., and Zhu, B.: Aerosol and boundary-layer interactions and impact on air quality, Natl. Sci. Rev., 4, 810–833, https://doi.org/10.1093/nsr/nwx117, 2017.

Lu, J., Nazarian, N., Hart, M. A., Krayenhoff, E. S., and Martilli, A.: Representing the effects of building height variability on urban canopy flow, Q. J. R. Meteorolog. Soc., 150, 46–67, https://doi.org/10.1002/qj.4584, 2024.

Menter, F. R., Kuntz, M., and Langtry, R.: Ten years of industrial experience with the SST turbulence model, Heat Mass Transfer, 2003.

https://doi.org/10.5194/egusphere-2026-2441
Preprint. Discussion started: 2 July 2026

Miller, S. J. and Gordon, M.: The measurement of mean wind, variances, and covariances from an instrumented mobile car in a rural environment, Atmos. Meas. Tech., 15, 6563–6584, https://doi.org/10.5194/amt-15-6563-2022, 2022.

Miller, S. J., Gordon, M., Staebler, R. M., and Taylor, P. A.: A study of the spatial variation of vehicle-induced turbulence on highways using measurements from a mobile platform, Boundary Layer Meteorol., 171, 1–29, https://doi.org/10.1007/s10546-018-0416-9, 2019.

Moat, B. I., Yelland, M. J., Pascal, R. W., and Molland, A. F.: An overview of the airflow distortion at anemometer sites on ships, Int. J. Climatol., 25, 997–1006, https://doi.org/10.1002/joc.1177, 2005.

Moat, B. I., Yelland, M. J., and Molland, A. F.: Quantifying the airflow distortion over merchant ships. Part II: Application of the model results, J. Atmos. Ocean. Technol., 23, 351–360, https://doi.org/10.1175/JTECH1859.1, 2006.

Mochida, A. and Lun, I. Y. F.: Prediction of wind environment and thermal comfort at pedestrian level in urban area, J. Wind Eng. Ind. Aerodyn., 96, 1498–1527, https://doi.org/10.1016/j.jweia.2008.02.033, 2008.

Mochida, A., Tabata, Y., Iwata, T., and Yoshino, H.: Examining tree canopy models for CFD prediction of wind environment at pedestrian level, J. Wind Eng. Ind. Aerodyn., 96, 1667–1677, https://doi.org/10.1016/j.jweia.2008.02.055, 2008.

Ramachandran, L., Ishak, I. A., Arafat, M., Zolpakar, N. A., Abidin, S. F. Z., and Harun, D. M.: Numerical analysis on the performance of aerodynamic devices on a car using CFD, Int. J. Integr. Eng., 16, 154–164, https://doi.org/10.30880/ijie.2024.16.06.015, 2024.

Seinfeld, J. H. and Pandis, S. N.: Atmospheric chemistry and physics: from air pollution to climate change, John Wiley & Sons, 1146 pp., 2016.

Straka, J. M., Rasmussen, E. N., and Fredrickson, S. E.: A mobile mesonet for finescale meteorological observations, J. Atmos. Oceanic Technol., 13, 921–936, https://doi.org/10.1175/1520-0426(1996)013%253C0921:AMMFFM%253E2.0.CO;2, 1996.

Wagner, T. J., Klein, P. M., and Turner, D. D.: A new generation of ground-based mobile platforms for active and passive profiling of the boundary layer, https://doi.org/10.1175/BAMS-D-17-0165.1, 2019.

Wu, H. and Agarwal, R. K.: Computational fluid dynamics study of modification to front wing endplate of FSAE race car for drag reduction, in: Aiaa Scitech 2023 Forum, AIAA Science and Technology (SciTech) Forum, AIAA 2023-1007, https://doi.org/10.2514/6.2023-1007, 2023.

Yang, Y., Zhang, Y., Han, T., Xie, C., Liu, Y., Huang, Y., Zhou, J., Sun, H., Zhao, D., Zhang, K., and Li, S.-M.: A correction algorithm for rotor-induced airflow and flight attitude changes during three-dimensional wind speed measurements made from a rotary unoccupied aerial vehicle, Atmos. Meas. Tech., 18, 3035–3050, https://doi.org/10.5194/amt-18-3035-2025, 2025.

Zajic, D., Fernando, H. J. S., Brown, M. J., and Pardyjak, E. R.: On flows in simulated urban canopies, Environ. Fluid Mech., 15, 275–303, https://doi.org/10.1007/s10652-013-9311-6, 2015.

Zhou, X., Yoon, S., Mara, S., Falk, M., Kuwayama, T., Tran, T., Cheadle, L., Nyarady, J., Croes, B., Scheehle, E., Herner, J. D., and Vijayan, A.: Mobile sampling of methane emissions from natural gas well pads in california, Atmos. Environ., 244, 117930, https://doi.org/10.1016/j.atmosenv.2020.117930, 2021.